Sharp Eccentric Rings in Planetless Hydrodynamical Models of Debris Disks

W. Lyra[1,2,3,4] & M. Kuchner[5]

[1]*NASA Jet Propulsion Laboratory, California Institute of Technology, 4800 Oak Grove Drive, Pasadena, CA 91109, USA*

[2]*California Institute of Technology, Division of Geological & Planetary Sciences, 1200 E California Blvd MC 150-21, Pasadena, CA 91125 USA*

[3]*Department of Astrophysics, American Museum of Natural History, 79th Street at Central Park West, New York, NY 10024, USA*

[4]*Carl Sagan fellow*

[5]*NASA Goddard Space Flight Center, Exoplanets and Stellar Astrophysics Laboratory, Code 667, Greenbelt, MD 21230, USA*

Exoplanets are often associated with disks of dust and debris, analogs of the Kuiper Belt in our solar system. These "debris disks" show a variety of non-trivial structures attributed to planetary perturbations and utilized to constrain the properties of the planets[1–3]. However, analyses of these systems have largely ignored the fact that, increasingly, debris disks are found to contain small quantities of gas[4–9], a component all debris disks should contain at some level[10,11]. Several debris disks have been measured with a dust-to-gas ratio around unity[4–9] where the effect of hydrodynamics on the structure of the disk cannot be ignored[12,13]. Here we report that dust-gas interac-

tions can produce some of the key patterns seen in debris disks that were previously attributed to planets. Through linear and nonlinear modeling of the hydrodynamical problem, we find that a robust clumping instability exists in this configuration, organizing the dust into narrow, eccentric rings, similar to the Fomalhaut debris disk[14]. The hypothesis that these disks might contain planets, though thrilling, is not necessarily required to explain these systems.

Disks around young stars appear to pass through an evolutionary phase when the disk is optically-thin and the dust-to-gas ratio ε ranges from 0.1 to 10. The nearby stars β Pictoris[5,6,15–17], HD32297[7], 49 Ceti[4], and HD 21997[9], all host dust disks resembling ordinary debris disks and also have stable circumstellar gas detected in molecular CO, Na I or other metal lines; the inferred mass of gas ranges from Lunar masses to a few Earth masses (see Supplementary Information, Sect 1). The gas in these disks is thought to be produced by planetesimals or dust grains themselves, via sublimation, photodesorption[10] or collisions[11], processes that should occur in every debris disk at some level.

Structures may form in these disk via a recently proposed instability[12,13]. Gas drag causes dust in a disk to concentrate at pressure maxima[18]; but when the disk is optically-thin to starlight, the gas is most likely primarily heated by the dust, via photoelectric heating. In this circumstance, a concentration of dust that heats the gas creates a local pressure maximum that in turn can cause the dust to concentrate more. The result of this photoelectric instability could be that the dust clumps into rings or spiral patterns or

other structures, that could be detected via coronographic imaging or other methods.

Indeed, images of debris disks and transitional disks show a range of asymmetries and other structures that beg for explanation. Traditionally, explanations for these structures rely on planetary perturbers – a tantalizing possibility. But so far, it has been difficult to prove that these patterns are clearly associated with exoplanets[19,20].

Previous investigations of hydrodynamical instabilities in debris disks neglected a crucial aspect of the dynamics: the momentum equations for the dust and gas. Equilibrium terminal velocities are assumed between time-steps in the numerical solution, and the dust distribution is updated accordingly. The continuity equation for the gas is not solved, i.e., the gas distribution is assumed to be time-independent, despite heating, cooling, and drag forces. Moreover, prior investigations only considered one-dimensional models, which can only investigate azimuthally-symmetric, ring-like patterns. This limitation also left open the possibility that in higher dimensions, the power in the instability might collect in higher azimuthal wavenumbers, generating only unobservable clumps.

We present simulations of the fully compressible problem, solving for the continuity, Navier-Stokes, and energy equations for the gas, and the momentum equation for the dust. Gas and dust interact dynamically via a drag force, and thermally via photoelectric heating. These are parametrized via a dynamical coupling time τ_f, and a thermal coupling time τ_T (see Supplementary Information, Sect 2). The simulations are performed with the Pencil Code[21–24], which solves the hydrodynamics on a grid. Two numerical

models are presented: (1) a threedimensional box embedded in the disk that co-rotates with the flow at a fixed distance from the star; and (2) a twodimensional global model of the disk in the inertial frame. In the former the dust is treated as a fluid, with a separate continuity equation. In the latter the dust is represented by discrete particles with position and velocities that are independent of the grid.

We perform a stability analysis of the linearized system of equations, that should help interpret the results of the simulations (see Supplementary Information, Sect 3). We plot in Fig. 1a-c the three solutions that show linear growth, as functions of ε and $n = kH$, where k is the radial wavenumber and H is the gas scale height (H=$c_s/\sqrt{\gamma}\Omega_k$, where c_s is the sound speed, Ω_k the Keplerian rotation frequency and γ the adiabatic index). The friction time τ_f is assumed to be equal to $1/\Omega_k$. The left and middle panels show the growth and damping rates. The right panels show the oscillation frequencies. There is no linear instability for $\varepsilon \geq 1$ or $n \leq 1$. At low dust load and high wavenumber the three growing modes appear. The growing modes shown in Fig. 1a have zero oscillation frequency, characterizing a true instability. The two other growing solutions (Fig. 1b-c) are overstabilities, given the associated non-zero oscillation frequencies. The pattern of larger growth rates at large n and low ε invites to take $\xi = \varepsilon n^2$ as characteristic variable, and explore the behavior of $\xi \gg 1$. The solutions in this approximation are plotted in Fig. 1f-g. The instability (red) has growth rate $\approx 0.26\,\Omega_K$ for all ξ. The overstability (yellow) reaches an asymptotic growth rate of $\Omega_K/2$, at ever growing oscillation frequencies. Damped oscillations (blue) occur at frequency close to the epicyclic frequency.

Whereas the inviscid solution has growth even for very small wavelengths, viscosity will cap power at this regime, leading to a finite fastest growing mode (see Supplementary Information, Sect 4), that we reproduce numerically (Fig. 1h). Though there is no linear growth for $\varepsilon \geq 1$, we show that there exists nonlinear growth for $\varepsilon = 1$. As seen in Fig. 1i, a qualitative change in the behaviour of the system (a bifurcation) occurs when the noise amplitude of the initial velocity ($u_{\rm rms}$) is raised enough, as expected from nonlinear instabilities[25,26]. This is an important result to emphasize because, depending on the abundance of H_2, the range of ε in debris disks spans both the linear and nonlinear regimes. The parameter space of τ_T and τ_f is explored in 1D models in the Supplementary Information (Sect 5), showing robustness.

In Fig. 2 we show the linear development and saturation of the photoelectric instability in a vertically stratified local box of size $(1 \times 1 \times 0.6)H$ and resolution 255 $\times$ 256 $\times$ 128. The dust and gas are initialized in equilibrium (see Supplementary Information, sect 6). The dust-to-gas ratio is given by $\log \varepsilon = -0.75$, so that there is linear instability, and viscosity $\nu = \alpha c_s H$ is applied as $\alpha = 10^{-4}$ (where α is a dimensionless parameter[27]). The initial noise is $u_{\rm rms}/c_s = 10^{-2}$. Fig. 2a shows the dust density in the x-z plane, and Fig. 2b in the x-y plane, both at 100 orbits. Fig. 2c shows the 1D x-dependent vertical and azimuthal average vs time. Via photoelectric heating, pressure maxima are generated at the locations where dust concentrates, that in turn attract more dust via the drag force. There is no hint of unstable short-wavelength ($< H$) nonaxisymmetric modes: the instability generates stripes. The simulation also shows that stratification does not quench the

instability. Fig. 2d shows the maximum dust density vs time, achieving saturation and steady state around 70 orbits.

We consider now a 2D global model. The resulting flow, in the $r - \phi$ plane (r is radius and ϕ is azimuth), is shown in Fig. 3a-c at selected snapshots. The flow develops into a dynamic system of narrow rings. Whereas some of the rings break into arcs, some maintain axisymmetry for the whole timespan of the simulation. It is also observed that some arcs later reform into rings. We check that in the absense of the drag force backreaction, the system does not develop rings (see Supplementary Information, Sect 7). We also check that when the conditions for the streaming instability[24] are considered, the photoelectric instability dominates (see Supplementary Information, Sect 8).

An interesting development of the model is that some of the rings start to oscillate, appearing eccentric. These oscillations are epicycles in the orbital plane, with a period equaling the Keplerian, corresponding to the free oscillations in the right hand side of Fig. 1a-c. We check (see Supplementary Information, Sect 9) that they correspond to eigenvectors for which $\boldsymbol{u} = \boldsymbol{v}$, that is, gas and dust velocities coinciding. For this mode, the drag force and backreaction are cancelled. So, for maintaining the eccentricity, this mode is being selected among the other modes in the spectrum. This is naturally expected when the dust-to-gas ratio is very high. For $\varepsilon \gg 1$, the gas is strongly coupled to the dust, canceling the gas-dust drift velocity in the same way that $\tau_f \ll 1$ does in the opposite way, by strongly coupling the dust to the gas. In this configuration, the freely

oscillating epicyclic modes can be selected.

We plot in Fig. 3e one of the oscillating rings, showing that its shape is better fit by an ellipse (red dotted line) than a circle (black dotted line). The eccentricity is 0.03, a value that is close to the eccentricity found[28] for the ring around HD 61005 (e=0.045 $\pm$ 0.015). We also notice that some of the clumps in Fig 3 should become very bright in reflected light, as they have dust enhancements of an order of magnitude. In conclusion, the proposed photoelectric instability provides simple and plausible explanations for rings in debris disks, their eccentricities, and bright moving sources in reflected light.

Recent work[29] suggests that the ring around Fomalhaut is confined by a pair of shepherding terrestrial mass planets, below the current detection imits. Detection of gas around the ring would be a way to distinguish that scenario from the one we propose. At present, only upper limits on the amount of gas in the Fomalhaut system exist[30]; they are relatively insensitive, however, because they probed CO emission, and CO could easily be dissociated around this early A type star.

1. Kuchner, M.J. & Holman, M.J. The Geometry of Resonant Signatures in Debris Disks with Planets. *Astrophys. J.*, **588**, 1110-1120, (2003).

2. Chiang, E., Kite, E., Kalas, P., Graham, J. & Clampin, M. Fomalhaut's Debris Disk and Planet: Constraining the Mass of Fomalhaut b from disk Morphology. *Astrophys. J.*, **693**, 734-749, (2009).

3. Lagrange, A.-M. et al. A Giant Planet Imaged in the Disk of the Young Star β Pictoris. *Science*, **329**, 57-60, (2010).

4. Zuckerman, B., Forveille, T., & Kastner, J. H. Inhibition of giant-planet formation by rapid gas depletion around young stars. *Nature*, **373**, 494-496, (1995).

5. Lagrange, A. et al. The beta Pictoris circumstellar disk. XXIV. Clues to the origin of the stable gas. *Astron. Astrophys.*, **330**, 1091-1108, (1998).

6. Roberge, A., Feldman, P.D., Weinberger, A.J., Deleuil, M., & Bouret, J-C. Stabilization of the disk around β Pictoris by extremely carbon-rich gas. *Nature*, **441**, 724-726, (2006).

7. Redfield, S. Gas Absorption Detected from the Edge-on Debris Disk Surrounding HD 32297. *Astrophys. J.*, **656**, L97-L100, (2007).

8. Maness, H. L., Fitzgerald, M. P., Paladini, R., Kalas, P., Duchene, G.,& Graham, J. R. CARMA Millimeter-Wave Aperture Synthesis Imaging of the HD 32297 Debris Disk. *Astrophys. J.*, **686**, L25-L28, (2008).

9. Moór, A. et al. Molecular Gas in Young Debris Disks. *Astrophys. J.*, **740**, L7-L12, (2011).

10. Grigorieva, A., Thebault, P., Artymowicz, P., & Brandeker, A. Survival of icy grains in debris discs. The role of photosputtering. *Astron. Astrophys.*, **475**, 755-764, (2007).

11. Czechowski, A., & Mann, I. Collisional Vaporization of Dust and Production of Gas in the β Pictoris Dust Disk. *Astrophys. J.*, **660**, 1541-1555, (2007).

12. Klahr, H. & Lin, D. N. C. Dust Distribution in Gas Disks. II. Self-induced Ring Formation through a Clumping Instability. *Astrophys. J.*, **632**, 1113-1121, (2005).

13. Besla, G. & Wu Y. Formation of Narrow Dust Rings in Circumstellar Debris Disks. *Astrophys. J.*, **655**, 528-540, (2007).

14. Kalas, P., Graham, J. R., & Clampin, M. A planetary system as the origin of structure in Fomalhaut's dust belt. *Nature*, **435**, 1067-1070, (2005).

15. Olofsson, G., Liseau, R., & Brandeker, A. Widespread Atomic Gas Emission Reveals the Rotation of the β Pictoris Disk. *Astrophys. J.*, **563**, L77-L80, (2001).

16. Brandeker, A., Liseau, R., Olofsson, G., & Fridlund, M. The spatial structure of the β Pictoris gas disk. *Astron. Astrophys.*, **413**, 681-691, (2004).

17. Troutman, M.R., Hinkle, K.H., Najita, J.R., Rettig, T.W. & Brittain, S.D. Ro-vibrational CO Detected in the β Pictoris Circumstellar Disk. *Astrophys. J.*, **738**, 12-19, (2011).

18. Takeuchi, T. & Artymowicz, P. Dust Migration and Morphology in Optically Thin Circumstellar Gas Disks. *Astrophys. J.*, **557**, 990-1006, (2001).

19. Janson, M., Carson, J. C., Lafrenière, D., Spiegel, D. S., Bent, J. R., & Wong, P. Infrared Non-detection of Fomalhaut b: Implications for the Planet Interpretation. *Astrophys. J.*, **747**, 116-122, (2012).

20. Currie, T., Debes, J., Rodigas, T. J., Burrows, A., Itoh, Y., Fukagawa, M., Kenyon, S. J., Kuchner, M., & Matsumura, S. Direct Imaging Confirmation and Characterization of a Dust-enshrouded Candidate Exoplanet Orbiting Fomalhaut. *Astrophys. J.*, **760**, L32-L37, (2012).

21. Brandenburg, A. & Dobler, W. Hydromagnetic turbulence in computer simulations. *CoPhC*, **147**, 471-475, (2002).

22. Lyra, W., Johansen, A., Klahr, H., & Piskunov, N. Global magnetohydrodynamical models of turbulence in protoplanetary disks. I. A cylindrical potential on a Cartesian grid and transport of solids. *Astron. Astrophys.*, **479**, 883-901, (2008).

23. Lyra, W., Johansen, A., Zsom, A., Klahr, H., & Piskunov, N. Planet formation bursts at the borders of the dead zone in 2D numerical simulations of circumstellar disks. *Astron. Astrophys.*, **497**, 869-888, (2009).

24. Youdin, A. & Johansen, A. Protoplanetary Disk Turbulence Driven by the Streaming Instability: Linear Evolution and Numerical Methods. *Astrophys. J.*, **662**, 613-626, (2007).

25. Stuart, J. T. Nonlinear stability theory. *Ann. Rev. Fluid Mech.*, **3**, 347-370, (1971).

26. Lesur, G. & Papaloizou, J. C. B. The subcritical baroclinic instability in local accretion disc models. *Astron. Astrophys.*, **513**, 60-71, (2010).

27. Shakura, N. I. & Sunyaev, R. A. Black holes in binary systems. Observational appearance. *Astron. Astrophys.*, **24**, 337-355, (1973).

28. Buenzli, E., Thalmann, C., Vigan, A., Boccaletti, A., Chauvin, G., Augereau, J. C., Meyer, M. R., Ménard, F., Desidera, S., Messina, S., Henning, Th., Carson, J., Montagnier, G., Beuzit, J. L., Bonavita, M., Eggenberger, A., Lagrange, A. M., Mesa, D., Mouillet, D., & Quanz, S. P. Dissecting the Moth: discovery of an off-centered ring in the HD 61005 debris disk with high-resolution imaging. *Astron. Astrophys.*, **524**, L1-L4, (2010).

29. Boley, A. C., Payne, M. J., Corder, S., Dent, W. R. F., Ford, E. B., & Shabram, M. Constraining the Planetary System of Fomalhaut Using High-resolution ALMA Observations. *Astrophys. J.*, **750**, L21-L24, (2012).

30. Liseau, R. Molecular line observations of southern main-sequence stars with dust disks: alpha PS A, beta Pic, epsilon ERI and HR 4796 A. Does the low gas content of the beta PIC and varepsilon ERI disks hint of planets? *Astron. Astrophys.*, **348**, 133-138, (1999).

Supplementary Information is linked to the online version of the the paper at www.nature.com/nature

Acknowledgments The writing of this paper started at the American Museum of Natural His-

tory, with financial support by the National Science Foundation under grant no. AST10-09802, and completed at the Jet Propulsion Laboratory, California Institute of Technology, under a contract with the National Aeronautics and Space Administration. This research was supported by an allocation of advanced computing resources supported by the National Science Foundation. The computations were performed on the Kraken system at the National Institute for Computational Sciences. We acknowledge discussions with H. Latter and G. Stewart.

Author Contributions W.L. contributed to developing the model, performed the calculations, and wrote the manuscript. M.K. contributed to developing the model and writing of the manuscript.

Author information Reprints and permissions information are available at www.nature.com/reprints. The authors declare no competing financial interests. Correspondence and requests should be addressed to W.L. (wlyra@jpl.nasa.gov) or M.K. (marc.j.kuchner@nasa.gov).

Figure 1 Linear analysis of the axisymmetric modes of the photoelectric instability. Solutions for axisymmetric perturbations $\psi' = \hat{\psi}\exp(st + ikx)$, where $\hat{\psi}$ is a small amplitude, x is the radial coordinate in the local Cartesian co-rotating frame, k is the radial wavenumber, t is time and s the complex frequency. Positive real s means that a perturbation grows, negative s that a perturbation is damped, and imaginary s represents oscillations. Solutions are for $\alpha = 0$, $\tau_f = 1/\Omega_K$, and $\tau_{_T}$=0. **a-e**, The five solutions as functions of $n = kH$ and ε. Solutions **a-c** show linear growth. Growth is restricted to the low dust-to-gas ratio ($\varepsilon < 1$), high wavenumber ($n > 1$) region. The growing modes in **b-c** have non-zero oscillation frequencies, characterizing an overstability. Conversely, solution **a** is a true instability. **d-e**, Solutions that correspond to damped oscillations through most of the parameter space. In a small region (high dust-to-gas ratio and high frequency), modes are exponentially damped without oscillating. **f-g**, Using $\xi = \varepsilon n^2$ and taking the limit $\xi \gg 1$ allows for better visualizing the three behaviors: true instability (red), overstability (yellow), and damped oscillations (blue). The other two solutions are the complex conjugate of the oscillating solutions, and not shown. **h**, When viscosity is considered ($\alpha = 10^{-2}$ in this example), power is capped at high wavenumber, leading to a finite most unstable wavelength. The figure shows the analytical prediction of the linear instability growth in this case (see Supplementary Information, Sect 4) compared to the growth rates measured numerically. The overall agreement is excellent. The growth rates are only very slightly underestimated. **i**, Although there is no linear instability for $\varepsilon = 1$, growth occurs when the amplitude of the initial perturbation ($u_{\rm rms}$) is increased, a hallmark of nonlinear

instability.

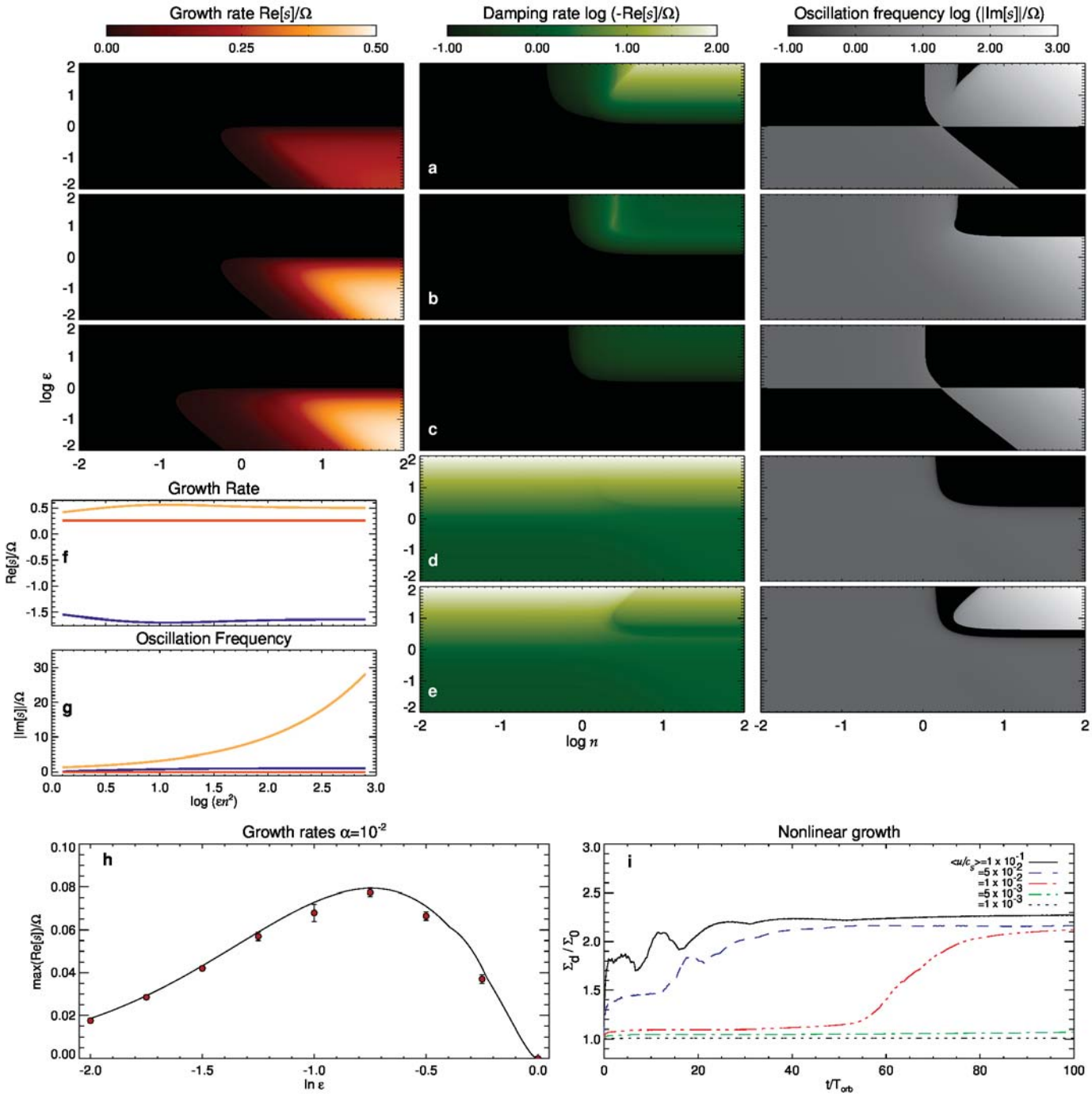

Figure 2 **Growth and saturation of the photoeletric instability.** In this threedimensional stratified local box with linearized Keplerian shear, the main source of heating is photoelectric. The equilibrium in the radial direction is between stellar gravity, Coriolis, and centrifugal forces. In the vertical direction the equilibrium for the gas is hydrostatic, between stellar gravity, pressure, and the drag force backreaction. To provide a stable stratification, an extra pressure $p_b = \rho c_b^2$ is added, where c_b is a sound speed associated with a background temperature. For the dust, a steady state is established between gravity, diffusion, and drag force. The dust continually falls to the midplane, but is diffused upwards. The diffusion is applied only in z, mimicking turbulent diffusion, that is in general anisotropic. **a**, $x-z$ cut at $y=0$ at 100 orbits. The instability concentrates dust in a preferred wavelength. The resulting structures have stable stratification. **b**, $x-y$ cut at the midplane $z=0$ at 100 orbits. No non-axisymmetric instability is observed, and the dust forms stripes. **c**, Time-evolution of the vertically and azimuthally averaged density, showing the formation of well-defined rings. **d**, Time evolution of the maximum dust density. The instability saturates at ≈70 orbits in this case. The slowdown compared to the growth rate $\Omega_K/2$ predicted in Fig. 1 is because of the use of viscosity, and the background pressure needed for the stratification. The dimensionless parameter $\beta = \gamma(c_b/c_s)^2$ measures the strength of this term. Panel **e** shows that linear instability exists as long as $\beta < 1$. The maximum growth rates drops smoothly from $\Omega_K/2$ for $\beta = 0$, to zero for $\beta = 1$. **f**, The structure formed in the dust density at $t = 50$ (≈8 orbits) for different values of beta. At moderate values of beta growth still occurs at a significant fraction of the dynamical time.

The run shown in panels **a-d** used β=0.5.

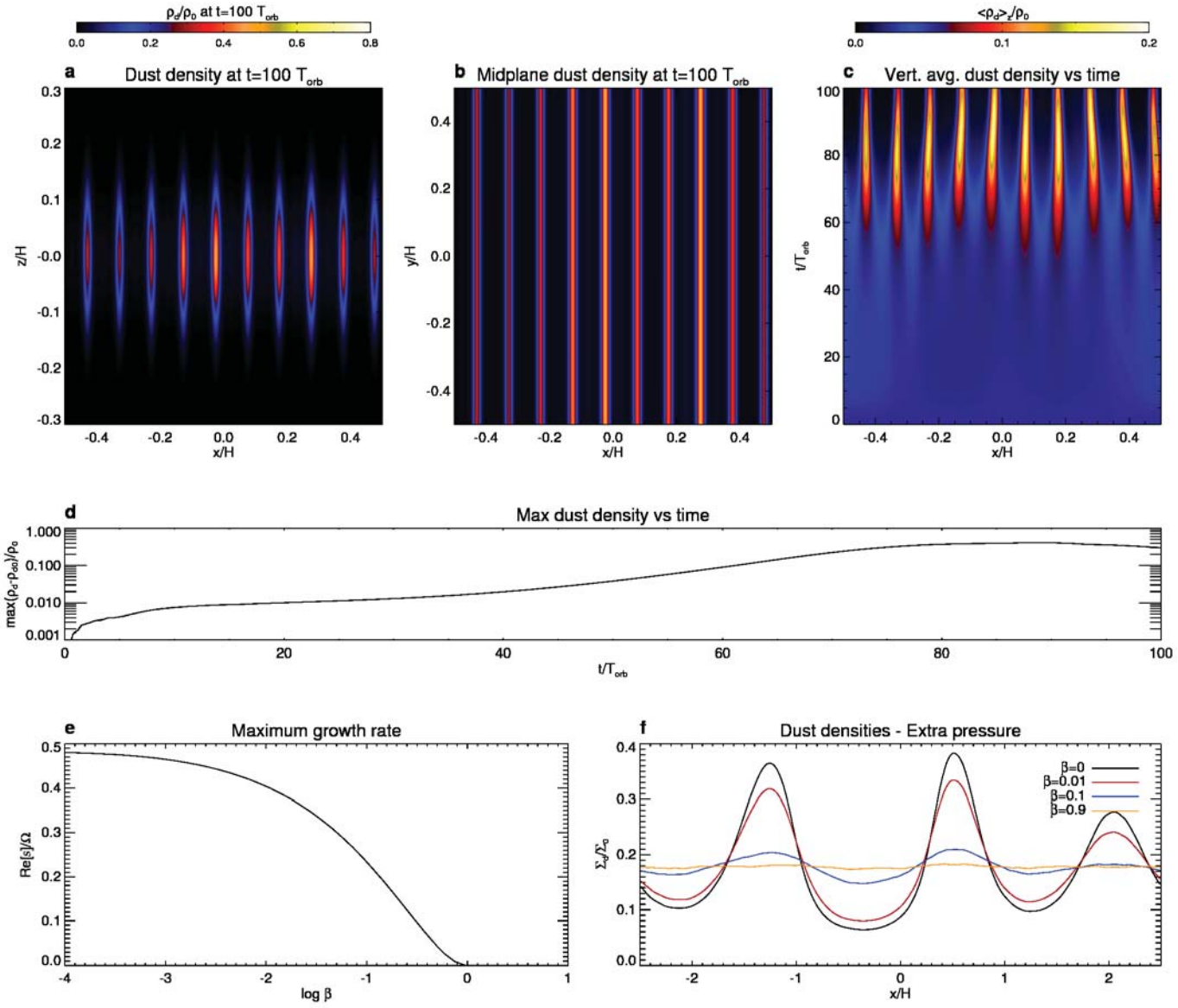

Figure 3 **Sharp eccentric rings. a-c**, Snapshots of the dust density in a twodimensional global disk in polar coordinates, at 20, 40, and 60 orbits, respectively. The photoelectric

instability initially concentrates the dust axisymmetrically into rings, at a preferred wavelength. As the simulation proceeds, some rings maintain the axisymmetry, others break into arcs. Some arcs rearrange into rings at later times, such as the ones at $r = 0.6$ and $r = 1.0$ between snapshots **b** and **c**. Though mostly axisymmetric, some rings appear to oscillate, appearing off-centered or eccentric. **d**, We measure the azimuthal spectral power of the density shown in snapshot c, as a function of radius. Modes from m=0 to m=3 are shown, where m is the azimuthal wavenumber. Though the ring at $r = 1.5$ has $m = 0$ as the more prominent mode, we show in panel **e** that a circle (black dotted line) is not a good fit. An ellipse of eccentricity $e = 0.03$ (red dotted line) is a better fit, though still falling short of accurately describing its shape. The black and red diamonds are the center of the circle (the star), and the center of the ellipse (a focal distance away from the star).

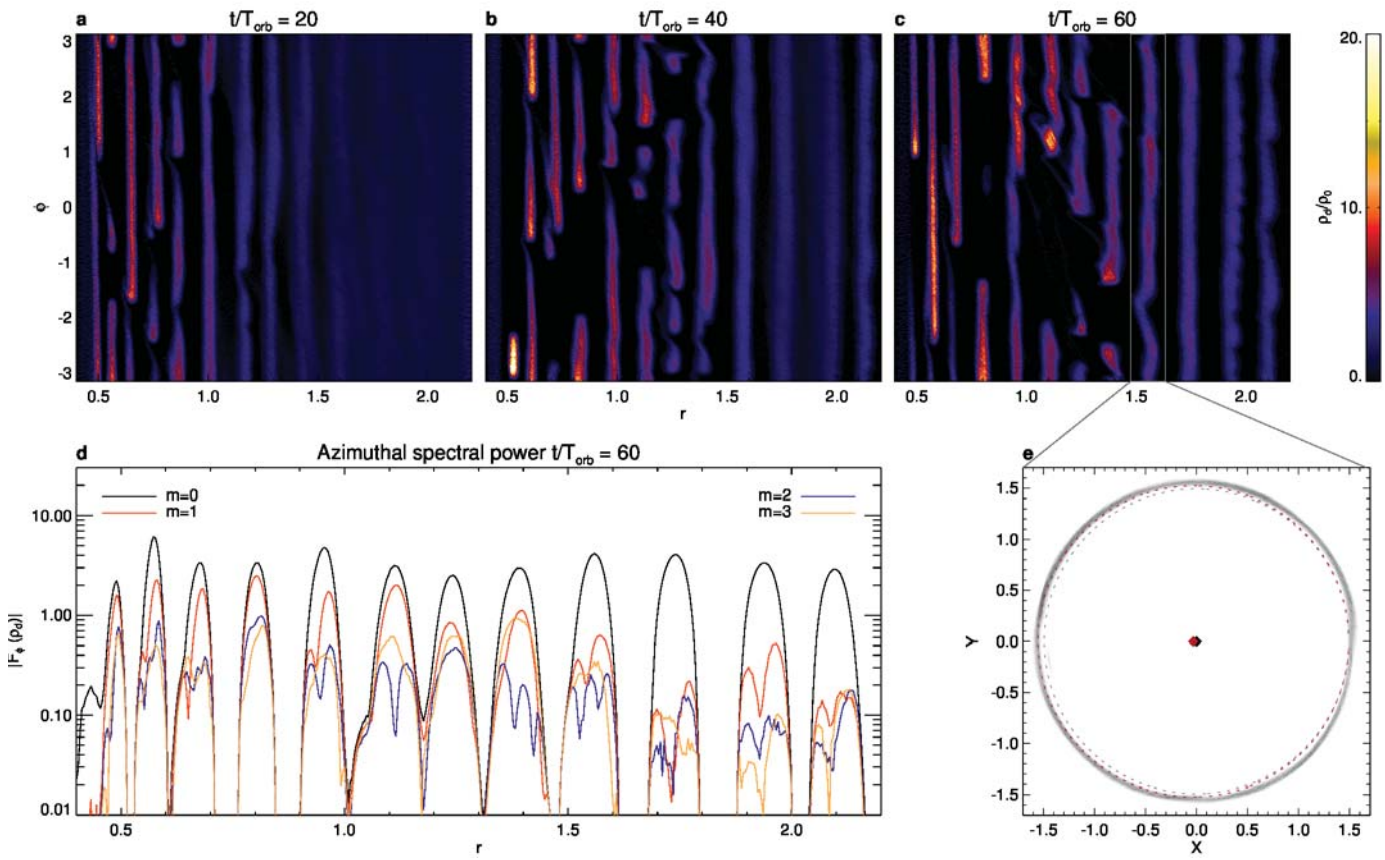
a
t/T_orb = 20
b
t/T_orb = 40
c
t/T_orb = 60
φ
r
ρ_d/ρ_0
d
Azimuthal spectral power t/T_orb = 60
m=0
m=1
m=2
m=3
|F_φ (ρ_d)|
r
e
X
Y

Supplementary Information

1 Gas in debris disks

Debris disks with gas represent a regime of nebular astrophysics that has only recently been quantified[31]. The archetype of the class, the best studied object so far, is the disk around β Pictoris, which we use as a reference point for our study.

1.1 Total gas mass

It is important to note that the total mass of gas that these debris disks have is poorly known, even for the well-studied disk around β Pictoris. Debris disk gas has mainly been observed in emission lines from metal ions and CO, but the bulk of the gas is generally assumed to be hydrogen, a component that is difficult to measure[32]. Estimates of the hydrogen abundance in the β Pictoris disk relative to the solar value range from 10^{-3} to 1; this range translates into a range of total gas mass from about $8 \times 10^{-4} M_\oplus$ to $0.8 M_\oplus$.

The dust mass is better constrained. Still, care must be taken to specify the particle size range of interest, since in typical grain size distributions, the larger bodies contain most of the mass, yet the smaller grains are the ones that we can detect. The disk should have a dust mass of $0.27 M_\oplus$ for particles smaller than 1 cm, assuming spherical grains with a number distribution $dn/da_\bullet \propto a_\bullet^{-3.5}$, where $a_\bullet$ is the grain radius[31]. Given these numbers, ε for β Pictoris would lie in the range of 0.3 to 300.

These numbers roughly span the range of parameters for other debris disks with gas, with 49 Ceti a notably gas-rich exception. Estimates for the HD 21997 disk[9] quote a dust mass of $\sim 0.1 M_\oplus$ and a gas mass of $0.35 M_\oplus$, corresponding to $\varepsilon \approx 0.3$. An upper limit to the gas mass of HD 3229 is estimated[7] at $\sim 0.3 M_\oplus$; the dust mass in the same system[8] lies in the range of 0.02–1 $M_\oplus$, yielding ε in the range ≈0.05–3. The 49 Ceti debris disk has about the same mass of dust as HD21997, but substantially more gas[4]: $13 M_\oplus$, corresponding to $\varepsilon \approx 0.008$.

1.2 Mean free path

To determine if the system may or may not be treated hydrodynamically, we estimate the mean free path

$$\lambda_{\rm mfp} \approx \frac{1}{\sigma_{\rm coll}\, n_g} \tag{1}$$

in actual systems. In Eq. (1) n_g is the number density of the constituent gas molecules or atoms, and $\sigma_{\rm coll} \approx 2 \times 10^{-15} {\rm cm}^{-2}$ the collisional cross section of hydrogen, taken to be representative.

For 49 Ceti, a best fit for the CO column density of $N_{\rm CO} = 4 \times 10^{15}\,{\rm cm}^{-2}$ at r =100 AU is reported[33]. The number density can be estimated from the column density, $n_g = N_g/2H$, where H is the gas scale height. For an aspect ratio $h = H/r = 0.02$, the midplane number density is $n_{\rm CO}$ = 70 cm^{-3} at 100 AU . This provides an upper limit to the mean free path of $\lambda_{\rm mfp} < 0.4$ AU. The actual mean free path is likely to be much lower, because of the presence of hydrogen. Assuming a hydrogen abundance up to $n_{\rm H_2}/n_{\rm CO} = 10^4$, the mean free path ranges from 4×10^{-5} to 0.4 AU. Considering typical ring structures of 10 AU, the lower limit is well within the hydrodynamical range, and even the upper limit implies marginal applicability.

For β Pictoris, observations report a column density of atomic C II of $10^{16}\,{\rm cm}^{-2}$ at ≈ 100 AU [6]. With aspect ratio h=0.2 [34], this translates into a number density of $\approx 20\,{\rm cm}^{-3}$ and thus an upper limit on the mean free path of ≈2 AU. Assuming solar composition ($n_{\rm H} \approx 10^3 {\rm cm}^{-3}$)[34], the mean free path should be $\lambda_{\rm mfp} = 0.03$ AU, well in the hydrodynamic limit.

For HD 21997, a simultaneous fit of the CO J=3-2 and J=2-1 lines[9] yields $n_{\rm CO} = 22 \pm 5$ cm^{-3} and $n_{\rm H_2}/n_{\rm CO}$=1000 $\pm$ 500 at 63 AU (the best fit of $n_{\rm CO} = 10$ cm^{-3} for the J=3-2 line assuming the canonical value $n_{\rm H_2}/n_{\rm CO} = 10^4$ gives a poor fit for the J=2-1 line). This inferred number density of $n_{\rm H_2} = 1.1 - 2.2 \times 10^4 {\rm cm}^{-3}$ for hydrogen places the mean free path at $\lambda_{\rm mfp} = 0.0015 - 0.003$ AU, also well within the hydrodynamic limit.

The situation for HD 32297 is less constrained, but limits can still be derived. The gas mass is estimated from Na instead of CO, with a column density of $N_{\rm NaI} \approx 10^{11}\,{\rm cm}^{-2}$. Assuming that the abundances are similar to those of β Pictoris[6], and using as constrains Na measurements[16] and H I upper limits[35], the hydrogen density should be $N_{\rm HI}/N_{\rm NaI} \approx 10^9$. For an aspect ratio h=0.1 at 100 AU [36], this yields a number density of $n_{\rm HI}$=$3 \times 10^5\,{\rm cm}^{-3}$, and thus a mean free path $\lambda_{\rm mfp} = 10^{-4}$ AU. Given the assumptions made, this is likely an overestimate. Nevertheless, given an integral scale of 10 AU, a revised value three orders of magnitude upward would still be in the range of applicability of hydrodynamics.

1.3 Thermal time

Another important quantity for the instability we investigate is the thermal time scale. In the model quoted[31], the dust is concentrated in a ring about 100-140 AU from the star. At the peak in the dust density, the midplane gas density is about 10 cm^{-3}, the dust temperature is roughly 100 K, the gas temperature is roughly 70 K. The gas is primarily heated by photoelectric emission from dust grains, and primarily cooled through the C II 157.7 μm line emission and the total heating/cooling power is roughly 2×10^{-19} erg s^{-1} cm^{-3}. Since the specific heat of molecular hydrogen at 70 K is roughly 1.3×10^8 erg g^{-1} K^{-1}, the thermal time scale in this model is about $0.5(n_{\rm H_2}/10\,{\rm cm}^{-3})$ years. Given the range of possible hydrogen abundances in the disk, the range of time scales of interest corresponds to about 10^{-4} to 0.1 orbital periods.

2 The model

We work primarily in the thin disk approximation, using the vertically integrated equations of hydrodynamics

$$\frac{\partial \Sigma_g}{\partial t} = -(\boldsymbol{u}\cdot\boldsymbol{\nabla})\,\Sigma_g - \Sigma_g \boldsymbol{\nabla}\cdot\boldsymbol{u} \tag{2}$$

$$\frac{\partial \boldsymbol{u}}{\partial t} = -(\boldsymbol{u}\cdot\boldsymbol{\nabla})\,\boldsymbol{u} - \frac{1}{\Sigma_g}\boldsymbol{\nabla} P - \boldsymbol{\nabla}\Phi - \frac{\Sigma_d}{\Sigma_g}\boldsymbol{f}_d \tag{3}$$

$$\frac{\partial S}{\partial t} = -(\boldsymbol{u}\cdot\boldsymbol{\nabla})\,S - \frac{c_v}{T}\frac{(T-T_p)}{\tau_{_T}}. \tag{4}$$

In these equations, Σ_g and Σ_d are the vertically integrated gas and dust densities, respectively; $\boldsymbol{u}$ stands for the velocity of the gas parcels, P is the vertically-integrated pressure, and Φ is the gravitational potential. $S = c_v\left(\ln P - \gamma \ln \Sigma_g\right)$ is the gas entropy, where c_v is the specific heat at constant volume and $\gamma = c_p/c_v$ is the adiabatic index, with c_p the heat capacity at constant pressure. T stands for the gas temperature. A tridimensional model is considered in Sect. 6.

The dust evolves Lagrangianly according to

$$\frac{d\boldsymbol{x}}{dt} = \boldsymbol{v} \tag{5}$$

$$\frac{d\boldsymbol{v}}{dt} = -\boldsymbol{\nabla}\Phi + \boldsymbol{f}_d \tag{6}$$

where $\boldsymbol{x}$ is the position of a dust particle and $\boldsymbol{v}$ its velocity. The gravitational potential is given by $\Phi = -GM_\star/r$, where G is the gravitational constant, $M_\star$ the stellar mass, and r the stellocentric distance. The pressure is given by $P = \Sigma_g c_s^2/\gamma$, where c_s is the sound speed.

The model is closed by specifying the drag force $\boldsymbol{f}_d$ by which gas and dust interact; and T_p, a simple prescription for the gas temperature set by photoelectric heating. These are given by

$$f_d = -\frac{(\boldsymbol{v}-\boldsymbol{u})}{\tau_f} \tag{7}$$

$$T_p = T_0\frac{\Sigma_d}{\Sigma_0}. \tag{8}$$

The quantities τ_f and $\tau_{_T}$ are the dynamical and thermal coupling times between gas and dust, respectively. They have a radial variance to match the Keplerian rate

Table 1: Symbols used in this work

Symbol	Definition	Description
t		time
$\boldsymbol{u}$, $\boldsymbol{v}$		gas and dust velocity
p, P		gas pressure (3D and vertically integrated)
ρ_g, Σ_p		volume and surface gas density
ρ_d, Σ_d		volume and surface dust density
S		entropy
c_v, c_p		heat capacity at constant volume and at constant pressure
T, T_p		gas and dust temperature
τ_T, τ_f		thermal relaxation and friction time
γ		adiabatic index
r, ϕ		radial polar coordinate, azimuth
c_s		sound speed
Ω		angular frequency
s, σ	$\sigma = s/\Omega$	complex eigenfrequency
k, n	$n = kH$	radial wavenumber, normalized radial wavenumber
m		azimuthal wavenumber
ν, α	$\nu = \alpha c_s H$	viscosity and Shakura-Sunyaev parameter
υ	υ=$\alpha\gamma n^2$	normalized viscosity
H	$H = c_s/\sqrt{\gamma}\Omega$	gas scale height
h	$h = H/r$	aspect ratio
H_d	$H_d = \sqrt{D/\zeta}$	dust scale height
ε		dust-to-gas ratio
c_b	$p_b = \rho_g c_b^2$	sound speed associated with background temperature
β	$\beta = \gamma\,(c_b/c_s)^2$	dimensionless background pressure parameter
D		dust diffusion coefficient
ζ	$v_z = -\zeta z$	proportionality factor in dust vertical velocity

$$\tau_f = \tau_{f0}\,\Omega_0/\Omega \tag{9}$$
$$\tau_T = \tau_{T0}\,\Omega_0/\Omega \tag{10}$$

where $\Omega = \sqrt{GM_\star/r^3}$ is the Keplerian angular frequency. The subscript "0" refers to the values of the quantities at an arbitrary reference radius r_0. The quantities τ_{f0} and τ_{T0} are free parameters of the model.

Given that the thermal time is sometimes expected to be very low (10^{-4} orbital periods, as estimated in Sect. 1.3) we also run models with instantaneous thermal coupling. For these models, we skip solving the energy equation, and equate $T = T_p$ according to Eq. (8). The sound speed is updated accordingly. This change effectively amounts to choosing a new equation of state that depends on the dust density

$$\lim_{\tau_T\to 0} P = c_v\,(\gamma-1)\,T_0\Sigma_g\Sigma_d/\Sigma_0. \tag{11}$$

A list of the mathematical symbols used in this work, together with their definitions, is provided in Table 1. We solve the equations with the PENCIL CODE [1], which integrates the evolution equations with sixth order spatial derivatives, and a third order Runge-Kutta time integrator. Sixth-order hyperdissipation terms are added to Eq. (2)-Eq. (4), to provide extra dissipation near the grid scale[22–23]. They are needed because the high order scheme of the Pencil Code has little overall numerical dissipation[37].

3 Linear stability analysis

We perform a linear stability analysis, that should assist on interpreting the results of the numerical simulations. To derive the perturbation equations, we make use of the shearing sheet and fluid approximations. The first treats the

[1]The code, including improvements done for the present work, is publicly available under a GNU open source license and can be downloaded at http://www.nordita.org/software/pencil-code

equations in a local, co-rotating Cartesian frame. The second greatly simplifies the treatment of solid particles by having a continuity equation. The 2D equations are

$$\begin{aligned}
\mathcal{D}_v\ \Sigma_d &= -\Sigma_d \boldsymbol{\nabla}\cdot\boldsymbol{v} && (12)\\
\mathcal{D}_v\ v_x &= 2\Omega v_y - \frac{1}{\tau_f}(v_x - u_x) && (13)\\
\mathcal{D}_v\ v_y &= -\frac{1}{2}\Omega v_x - \frac{1}{\tau_f}(v_y - u_y) && (14)\\
\mathcal{D}_u\ \Sigma_g &= -\Sigma_g \boldsymbol{\nabla}\cdot\boldsymbol{u} && (15)\\
\mathcal{D}_u\ u_x &= 2\Omega u_y - \frac{1}{\Sigma_g}\frac{\partial P}{\partial x} - \frac{\varepsilon}{\tau_f}(u_x - v_x) && (16)\\
\mathcal{D}_u\ u_y &= -\frac{1}{2}\Omega u_x - \frac{1}{\Sigma_g}\frac{\partial P}{\partial y} - \frac{\varepsilon}{\tau_f}(u_y - v_y) && (17)
\end{aligned}$$

where $\varepsilon = \Sigma_d/\Sigma_g$ is the dust-to-gas ratio and

$$\mathcal{D}_w = \partial_t + \boldsymbol{w}\cdot\boldsymbol{\nabla} - q\Omega x\partial_y \quad (18)$$

is the shear-modified advective derivative[38,39], with $q = 3/2$ the Keplerian shear rate. Upon linear decomposition $\psi = \psi_0 + \psi'$ and considering axis-symmetric planar wave perturbations $\psi' = \hat{\psi}\exp(st + ikx)$, these equations become

$$\begin{aligned}
s\hat{\Sigma}_d &= -\Sigma_{d0} ik \hat{v}_x && (19)\\
s\hat{v}_x &= 2\Omega\hat{v}_y - \frac{1}{\tau_f}(\hat{v}_x - \hat{u}_x) && (20)\\
s\hat{v}_y &= -\frac{1}{2}\Omega\hat{v}_x - \frac{1}{\tau_f}(\hat{v}_y - \hat{u}_y) && (21)\\
s\hat{\Sigma}_g &= -\Sigma_{g0} ik \hat{u}_x && (22)\\
s\hat{u}_x &= 2\Omega\hat{u}_y - \mathcal{C} ik(\hat{\Sigma}_d + \varepsilon\hat{\Sigma}_g) - \frac{\varepsilon}{\tau_f}(\hat{u}_x - \hat{v}_x) && (23)\\
s\hat{u}_y &= -\frac{1}{2}\Omega\hat{u}_x - \frac{\varepsilon}{\tau_f}(\hat{u}_y - \hat{v}_y) && (24)
\end{aligned}$$

where we used the instantaneous thermal coupling approximation (Eq. 11) to substitute

$$\boldsymbol{\nabla} P = \frac{c_{s0}^2}{\gamma\,\Sigma_0}(\Sigma_g\boldsymbol{\nabla}\Sigma_d + \Sigma_d\boldsymbol{\nabla}\Sigma_g). \quad (25)$$

Equations (19) and (22) readily allow for reducing the system to only four equations. We substitute these in the radial equation for gas velocity to obtain

$$\begin{aligned}
\sigma\hat{v}_x &= 2\hat{v}_y - \frac{1}{\Omega\tau_f}(\hat{v}_x - \hat{u}_x) && (26)\\
\sigma\hat{v}_y &= -\frac{1}{2}\hat{v}_x - \frac{1}{\Omega\tau_f}(\hat{v}_y - \hat{u}_y) && (27)\\
\sigma\hat{u}_x &= 2\hat{u}_y - \varepsilon\left(\frac{1}{\Omega\tau_f} + \frac{n^2}{\sigma}\right)\hat{u}_x + \varepsilon\left(\frac{1}{\Omega\tau_f} - \frac{n^2}{\sigma}\right)\hat{v}_x && (28)\\
\sigma\hat{u}_y &= -\frac{1}{2}\hat{u}_x - \frac{\varepsilon}{\Omega\tau_f}(\hat{u}_y - \hat{v}_y) && (29)
\end{aligned}$$

where we also substituted the normalizations

$$\begin{aligned}
\sigma &= s/\Omega && (30)\\
n &= kc_{s0}/\sqrt{\gamma}\Omega = kH && (31)
\end{aligned}$$

We now substitute $\tau_f = 1/\Omega$ so that the dispersion relation becomes simpler yet still captures the physically interesting case of the most mobile dust. We solve the eigenvalue problem

$$(\mathbf{M} - \mathbf{I}\sigma) \cdot \mathbf{\Lambda} = 0 \tag{32}$$

where $\mathbf{\Lambda} = (\hat{v}_x, \hat{v}_y, \hat{u}_x, \hat{u}_y)^T$, $\mathbf{I}$ is the unit matrix, and

$$\mathbf{M} = \begin{bmatrix} -1 & 2 & 1 & 0 \\ -1/2 & -1 & 0 & 1 \\ \varepsilon(1 - n^2/\sigma) & 0 & -\varepsilon(1 + n^2/\sigma) & 2 \\ 0 & \varepsilon & -1/2 & -\varepsilon \end{bmatrix}. \tag{33}$$

The dispersion relation for this linear system is a quintic polynomial

$$A\sigma^5 + B\sigma^4 + C\sigma^3 + D\sigma^2 + E\sigma + F = 0 \tag{34}$$

with coefficients

$$\begin{aligned} A &= 1, & (35)\\ B &= 2\varepsilon + 2, & (36)\\ C &= \varepsilon^2 + \varepsilon(n^2 + 2) + 3, & (37)\\ D &= \varepsilon^2 n^2 + \varepsilon(3n^2 + 2) + 2, & (38)\\ E &= \varepsilon^2(2n^2 + 1) + \varepsilon(3n^2 + 2) + 2, & (39)\\ F &= \varepsilon^2 n^2 - \varepsilon n^2. & (40) \end{aligned}$$

Eq. (34) has five solutions. Since quintics do not have a complete analytical solution, we solve it numerically at first, to explore the behavior of the solutions. The result is detailed in the main article, and plotted in Fig 1a-e. In the main article we also explore the limit of large n and low ε. Substituting $\xi = \varepsilon n^2$ as characteristic variable, and taking the limit $\xi \gg 1$, the coefficients are

$$\begin{aligned} A = 1; \quad B = 2; \quad C = \xi; \\ D = 3\xi; \quad E = 3\xi; \quad F = -\xi. \end{aligned} \tag{41}$$

The solutions are plotted in Fig 1f-g of the main article.

4 Comparing linear theory and simulations

From the solutions (Fig 1a-c of main article), we see that there is significant growth even for very small wavelengths. The simulations, however, will cap power at and near the grid scale. To make for a meaningful comparison, we add artificial Laplacian viscosity ν to the gas and dust momentum equations. The extra term in Fourier space is proportional to νk^2, which, using the alpha-viscosity recipe[27] $\nu = \alpha c_s H$, normalizing by Ω, and substituting Eq. (31), reduces to $v = \alpha\gamma n^2$. This enters in the coefficient matrix as diagonal terms. The new, viscous, system is therefore

$$[\mathbf{M} - \mathbf{I}(\sigma + v)] \cdot \mathbf{\Lambda} = 0 \tag{42}$$

We set $\alpha = 10^{-2}$ and solve the system numerically. Fig 1h of the main article shows a comparison between the linear growth rates predicted by Eq. (42), and the ones we measure by solving the system in the shearing sheet with fluid approximation (Eqs. (12) and (17)) with the Pencil Code, applying a small amplitude perturbation ($u_{\rm rms} = 10^{-3} c_s$). The agreement is excellent, with the measured growth rates only very slightly systematically offset from the analytical prediction.

5 Nonlinear numerical simulations

5.1 Numerical results and Robustness

5.1.1 The instability in one dimension

To understand the nature of the instability, it is instructive to consider it first in one-dimensional models, since it allows a more thorough exploration of the parameter space. We also shut down the drag force backreaction, in order

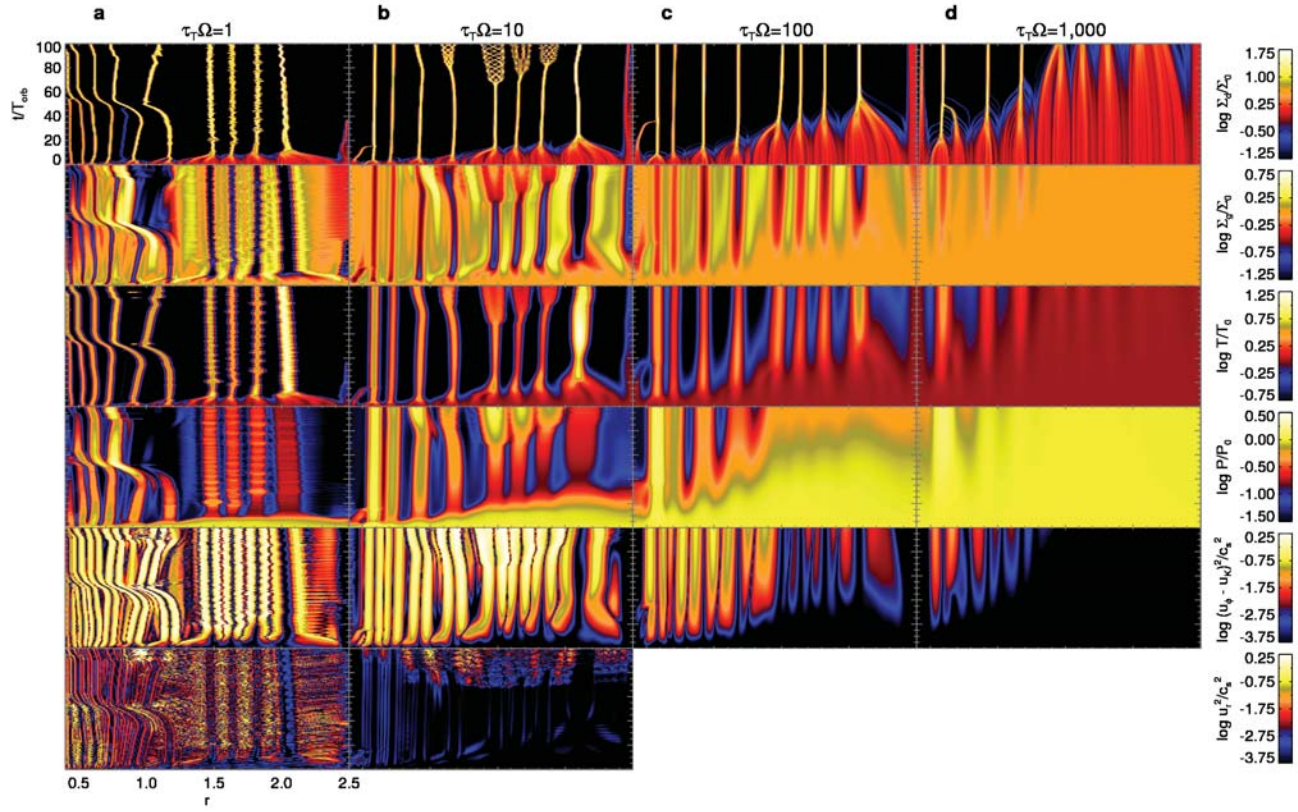

Supplementary Figure 1: Parameter space exploration for the thermal coupling time τ_{T0} in models with τ_{f0}=1 and without backreaction. **a**, The pressure build-up associated with too short thermal coupling time leads to modification of the centrifugal balance experienced by a gas parcel. **b**, In the case of τ_T=10 the pressure buildup leads to supersonic motion and consequent disruption of the dust fingers into a turbulent pattern. **c-d**, The models with larger τ_{T0} are better behaved as the buildup is slow. After long enough times (not shown) they too develop shock waves that disturb the dust streams. The dynamics is considerably different in models including back-reaction (Suppl. Fig. 3).

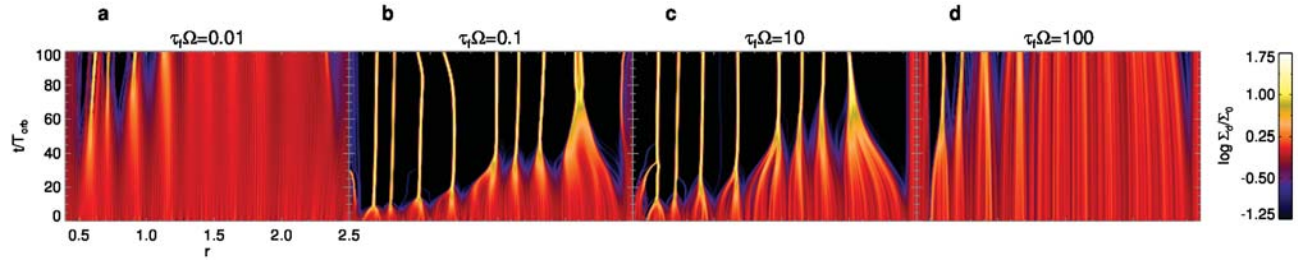

Supplementary Figure 2: Parameter space exploration for the friction time τ_{f0} in models with τ_{T0}=10 and without backreaction. There is an apparent symmetry with respect to $\tau_f = 1$. **a-b**, As the dust couples more strongly (lower τ_f), a grain takes longer to move away from the density maxima (pressure minima) into the pressure maxima. **c-d**, As the dust decouples (larger τ_f) the particles take longer times to move to the local pressure maxima. The velocities never get too close to sonic so turbulent disruption as in the case of short thermal coupling time does not occur.

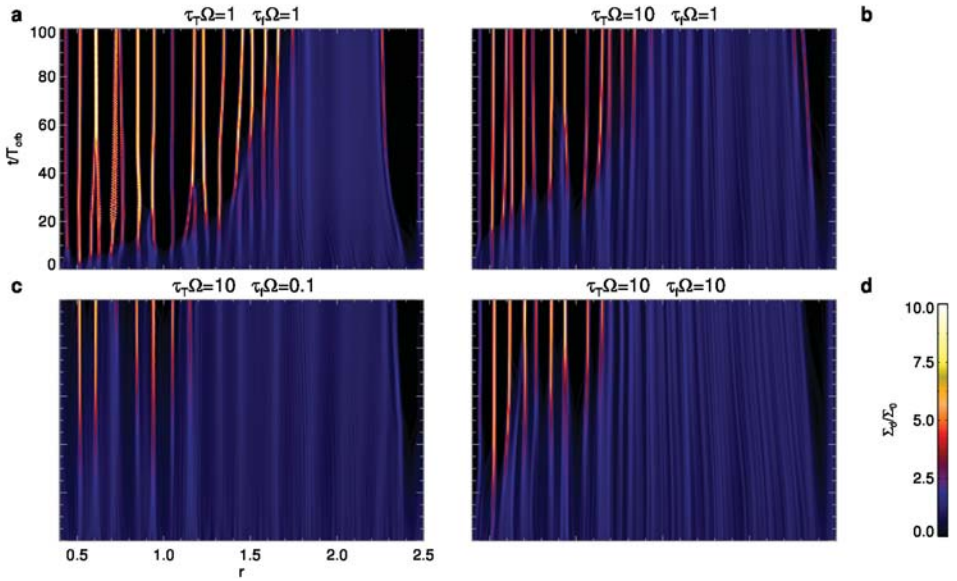

Supplementary Figure 3: The effect of the backreaction of the drag force is illustrated above. **a-b**, Space-time variation of the dust density in models of constant friction time and varying thermal time. **c-d**, Models of varying friction time and constant thermal time. Compared to the same models without backreaction (Suppl. Fig. 1 and Suppl. Fig. 2), we see that the dust streams are better shepherded. This is because when radial velocities are excited, the drag force backreaction damps them back to zero at an e-folding time $\tau_f\ \Sigma_g/\Sigma_d$. The shepherding of the dust stream should occur as long as this quantity is smaller or similar to τ_T.

to better isolate the effect of heating (but as we show later, this term will become of paramount importance in the phenomenology of debris disks in the presence of gas). It is illustrated in the Fig. 1 of the main article how the initial random overdensities quickly grow into massive accumulations of dust. We explore here the parameter space of the thermal coupling time τ_T and the dynamical coupling time τ_f. The dust-to-gas ratio is set to ε=1, so the regime is marginally nonlinear. We use Lagrangian particles for the dust.

Models exploring the parameter space of $\tau_T\Omega$ are shown in Suppl. Fig. 1. The panels from left to right correspond to $\tau_T\Omega$=1, 10, 1000, and 1000. The friction time was kept constant at $\tau_f\Omega$=1 so that the dust is mobile. In all cases the dust concentrates.

The models shown in Suppl. Fig. 1 contain some interesting features worth highlighting. As seen in the model of $\tau_T\Omega$=1.0, there are instances in time, around 30 orbits, that the dust distribution rapidly migrates inwards, setting in another equilibrium location. In the model with $\tau_T\Omega$=10 the dust at later times, around 50 orbits, passes from a thin stream to a shower, resembling the transition to turbulence seeing in, e.g., cigarette smoke. Both effects seem to be related to the pressure buildup. As the dust concentrates, the local temperature rises, leading to further dust buildup. The runaway process has to saturate at some point, and these effects seem to be manifestations of saturation. The pressure buildup leads to a gradual change in the centrifugal equilibrium $r\dot{\phi}^2 = r\Omega_K^2 + \Sigma_g^{-1}\,\partial_r P$. At some point the buildup of pressure significantly changes that relation, and the disk readjusts. In the other case, the buildup of pressure leads to supersonic speeds. Shock waves develop, leading to the disruption of the dust stream. These effects will be significantly mitigated by the inclusion of the drag force backreaction, in Sect. 5.1.3.

5.1.2 Effect of gas drag

The models shown in the previous section were run with a fixed friction time of $\tau_f\Omega$=1, representing the most mobile particles. We consider now models with varying τ_f, keeping $\tau_T\Omega$=10. A suite of such models is shown in Suppl. Fig. 2. As the dust decouples (larger τ_f), it takes longer for the pressure gradient to move the particles to the pressure maxima. As the dust couples more strongly (lower τ_f), it takes longer for the dust to decouple itself from the density maxima (pressure minima) and into the pressure maxima. The symmetry with respect to $\tau_f\Omega = 1$ is striking.

In the extreme of particle tracers ($\tau_f = 0$) there is no instability as the gas and dust cannot get separated. The heating leads to expansion, that carries away the dust, leading to cooling. The process is self-regulated. In the opposite extreme of decoupled dust $\tau_f \to \infty$ there is no instability either as the dust does not get pushed toward pressure maxima.

5.1.3 Effect of gas drag back-reaction

We now turn to the effect of the last term in the right hand side of the momentum equation, the drag force backreaction from the particles onto the gas. We re-run models of $\tau_T\Omega$=1 and 10, with τ_{f0}=1 (the leftmost ones in Suppl. Fig. 1), but now including this term. The results are shown in the upper panels of Suppl. Fig. 3, for the dust density only. Comparing these models with the ones without back-reaction shown in Suppl. Fig. 1, we see that the jerks in position are absent, as well as the dispersion of the particles into turbulent streams as seen in the models without backreaction. In other words, the backreaction of the drag force has the effect of shepherding the dust streams.

The reason is because in the other models, although the dust is forced to follow the gas, the gas is unconstrained by the dust. When backreaction is included, the gas follows the dust whenever the dust-to-gas ratio ε is high. When $\varepsilon >\sim 1$ the backreaction partially dominating the gas motion effectively herds the dust; a linear perturbation to the system executes exponentially damped oscillations, as shown in Fig. 1 of the main article. This effect will become important, in higher dimensions, on damping non-axisymmetric modes and confining the dust concentration into rings instead of clumps.

Interestingly, this effect, being proportional to τ_f, should break the symmetry with respect to $\tau_f = 1$ seen in the models without backreaction (Suppl. Fig. 2). Indeed, this is what is seen in the lower panels of Suppl. Fig. 3, where we show the result of two simulations with τ_T=10 and backreaction included, varying τ_f. The left panel has $\tau_f = 0.1$ and the right panel has $\tau_f = 10$. The simulation with shorter friction time experiences less clumping for the same thermal coupling time.

The herding provided by the drag force also introduces a dependency on τ_T/τ_f, because if $\tau_T \ll \tau_f$, the pressure builds much faster than the dust can respond.

6 Three dimensions and stratification

We assess now the impact of three-dimensionality and stratification in the instability. We need first to establish the condition of vertical hydrostatic equilibrium. We treated so far the gas-dust debris disks as a system where the only source of heating was photoelectric, which leads to the equation of state Eq. (11) under instantaneous thermal coupling. This is a suitable approximation for one-dimensional models as in the radial direction it is the centrifugal force that balances gravity. However, in the vertical direction, as pressure plays the central role of establishing hydrostatic equilibrium against stellar gravity, photoelectric heating alone cannot sustain the gas column. Extra sources of pressure must be considered.

6.1 Extra pressure

We add to the equation of state a term that embodies a background temperature T_b, not associated with the dust, from, e.g., H_2 photodissociation, H_2 formation, and H_2 collisional de-excitation. For simplicity, we consider this background temperature constant. This temperature will enter the equation of state as an extra isothermal term. For reasons of symmetry, we can define a "background sound speed" c_b associated with this temperature, and thus write $p_b = \rho_g c_b^2$. The full pressure is thus

$$p = \rho_g c_b^2 + p(\rho_d). \tag{43}$$

The term $p(\rho_d) \propto \rho_g\rho_d$ is the 3D equivalent to Eq. (11). We assess the effect of the extra background pressure in the photoelectric instability. For the axisymmetric modes, this term contributes an extra pressure force to be added to the u_x perturbation equation. The linear system then becomes

$$\mathbf{M} = \begin{bmatrix} -1 & 2 & 1 & 0 \\ -1/2 & -1 & 0 & 1 \\ \varepsilon(1-n^2/\sigma) & 0 & -(\varepsilon+\beta)(n^2/\sigma)-\varepsilon & 2 \\ 0 & \varepsilon & -1/2 & -\varepsilon \end{bmatrix}. \tag{44}$$

where

$$\beta = \gamma\left(\frac{c_b}{c_s}\right)^2 \tag{45}$$

is a dimensionless normalization. The dispersion relation is not much different. It is also a quintic polynomium, with coefficients

$$A = 1 \quad (46)$$
$$B = 2\varepsilon + 2 \quad (47)$$
$$C = n^2\beta + \varepsilon(n^2+2) + \varepsilon^2 + 3 \quad (48)$$
$$D = \varepsilon(n^2(\beta+3)+2) + 2n^2\beta + \varepsilon^2 n^2 + 2 \quad (49)$$
$$E = \varepsilon(n^2(\beta+3)+2) + 2n^2\beta + \varepsilon^2(2n^2+1) + 2 \quad (50)$$
$$F = \varepsilon n^2(\beta-1) + \varepsilon^2 n^2. \quad (51)$$

These coefficients resume to Eqs. (34)–(40) for $\beta = 0$. We show in Fig 2e of the main article the maximum growth rate as a function of β. The linear instability weakens as β increases, eventually disappearing when $\beta = 1$. For $\beta = 0.1$ the maximum growth rate is approximately half as that for $\beta = 0$, so the instability still occurs at timescales comparable to the dynamical time. We show the growth for different modes in Fig 2f of the main article. There are no major differences qualitatively. The modes for higher β develop similar structures at a slower pace. We conclude that linear instability exists as long as photoelectric heating dominates over other heating processes.

6.2 Stratification

We assess now the impact of stratification in the instability. We start by finding the equilibrium structure of the dust sub-disk in the z-direction[40,41].

6.3 Dust steady state

Like in gas-rich protoplanetary disks, the dust, once decoupled, will starting settling toward the midplane of the disk, obeying the z-momentum equation

$$\mathcal{D}_v\, v_z = -\Omega^2 z - \frac{1}{\tau_f}(v_z - u_z). \quad (52)$$

Since the dust is pressureless, when $v_z = 0$ and $u_z = 0$ equilibrium is only possible if $z = 0$, i.e., the dust concentrates in an infinitely thin midplane layer. Support against gravity comes from $v_z \neq 0$, so the dust is not in equilibrium, but in a steady state, defined by setting $\partial_t = 0$ in the above equation. We also assume $\partial_y = u_z = 0$, leading to

$$v_z \partial_z v_z = -\Omega^2 z - \tau_f^{-1} v_z \quad (53)$$

The ansatz $v_z = -\zeta z$ yields the quadratic equation $\zeta^2 - \zeta/\tau_f + \Omega^2 = 0$, so

$$\zeta = \left(\tau_f^{-1} \pm \sqrt{\tau_f^{-2} - 4\Omega^2}\right)/2. \quad (54)$$

Real solutions exist for $\tau_f \leq 1/2\Omega$. The ansatz $v_z = -\zeta z$ means that matter is constantly falling toward the midplane. The non-zero divergence would unboundedly increase the density, if not counterbalanced by some mechanism. That mechanism is diffusion. The continuity equation for the dust is rewritten

$$\mathcal{D}_v\, \rho_d = -\rho_d \boldsymbol{\nabla}\cdot\boldsymbol{v} + D\nabla^2\rho_d \quad (55)$$

so that a steady state is possible, in which the infall of dust towards the midplane is balanced by diffusion away from it, leading to the differential equation

$$D\partial_z^2\rho_d + \zeta z \partial_z \rho_d + \zeta\rho_d = 0. \quad (56)$$

This equation has a general solution

$$f(z) = C_1 \exp\left(-\frac{\zeta z^2}{2D}\right)\left[1 + C_2\sqrt{\frac{\pi D}{2\zeta}}\ \mathrm{erfi}\left(z\sqrt{\frac{\zeta}{2D}}\right)\right], \quad (57)$$

where erfi is the imaginary error function. Because this function diverges at infinity where the density should tend to zero, the solution requires C_2=0. We are thus left only with a Gaussian

$$\rho_d = \mathrm{Re}\,[f(z)] = \rho_{d0}\exp\left(-\frac{z^2}{2H_d^2}\right). \quad (58)$$

with $H_d = \sqrt{D/\zeta}$ the dust scale height.

6.4 Gas hydrostatic equilibrium

We now derive the equilibrium condition of the pressure-supported gas column, which follows from the gas z-momentum equation

$$\mathcal{D}_u\, u_z = -\Omega^2 z - \frac{1}{\rho}\frac{\partial p}{\partial z} - \frac{\varepsilon}{\tau_f}(u_z - v_z). \tag{59}$$

Setting $u_z = 0$ and substituting $v_z = -\zeta z$, we are left with the following condition of hydrostatic equilibrium

$$\frac{1}{\rho}\frac{\partial p}{\partial z} = -\left(\Omega^2 - \frac{\varepsilon\zeta}{\tau_f}\right) z \tag{60}$$

Given $v_z = -\zeta z$, $\ln\rho_d = -z^2/2H_d^2$, and $u_z = 0$, we calculate ρ_g that satisfies the equilibrium condition. Substituting the equation of state and $\varepsilon = \rho_d/\rho$ (now a function of z), we arrive at the following equation

$$\frac{1}{\rho}\left[\frac{\partial\rho}{\partial z}(c_b^2 + \mathcal{C}\rho_d) + \frac{\rho_d\zeta z}{\tau_f}\right] = -\left(\Omega^2 - \frac{\mathcal{C}\rho_d}{H_d^2}\right) z, \tag{61}$$

where $\mathcal{C} = c_{s0}^2/(\gamma\rho_0)$. The equation above can be cast in the form

$$\frac{1}{y}\left[y'(a + b\,e^{-z^2/2c}) + dz\,e^{-z^2/2c}\right] = -z\left(f - \frac{b}{c}\,e^{-z^2/2c}\right), \tag{62}$$

where $y = \rho$, $a = c_b^2$, $b = \mathcal{C}\varepsilon_0$ $c = H_d^2$, $d = \rho_{d0}\zeta/\tau_f$ and $f = \Omega^2$. The various parameters are associated with different physical mechanisms involved in the equilibrium: a is associated with support from the background pressure, b from photoelectric heating, and c from diffusion; d is related to the drag force backreaction, and f to gravity. The general solution for Eq. (62) is

$$y(z) = F(d) + K_1 e^{z^2/2c}\left(a e^{z^2/2c} + b\right)^{-(1+cf/a)}. \tag{63}$$

For no dust backreaction (d=0) and no photoelectric heating ($b = 0$) it resumes to the usual isothermal stratification

$$y(z) = K_2\, e^{-fz^2/2a} = \rho_0 e^{-z^2/2H_g^2} \tag{64}$$

with $H_g = c_b/\Omega$. The term containing d is

$$F(d) = \frac{dc}{b(1-\chi)}\;\; \psi(1+\psi)^{-(1+\chi)} \;\; {}_2F_1\left(-\chi,\, 1-\chi;\, 2-\chi; -\psi\right) \tag{65}$$

where $\psi = b/a\; e^{-z^2/2c}$, $\chi = fc/a = \Omega^2 H_d^2/c_b^2$ and ${}_2F_1$ is the hyper-geometric function.

We show in Suppl. Fig. 4 the resulting stratification given the same dust distribution (H_d=0.5, ζ=1, τ_f=0.5). The dark yellow line shows the usual isothermal stratification. The blue line shows the effect of adding the photoelectric heating. The reduction in gas mass is because, with the extra pressure, less mass is needed to balance the stellar gravity. The reduction in mass in the center stems from the higher temperature at the dust peak. The red line adds the effect of the drag force backreaction. It raises the gas mass profile because it behaves as extra gravity, as dust falls onto the midplane dragging the gas with it. We test numerically that this equilibrium is stable.

The model shown in Fig 2a-d of the main article had box length $(1 \times 1 \times 0.6)H$, resolution $255 \times 256 \times 128$, $\zeta = 1$ (that is, $v_z = -z$, which sets $\tau_f = 0.5$, according to Eq. (54)). The background temperature was set as $\beta = 0.5$ for the background pressure, with $c_{s0} = 1$ for the photoelectric pressure, and dust-to-gas ratio $\log\varepsilon = -0.75$, so that there is linear instability. The box is started with linear noise at the percent level. The dust diffusion coefficient was $D = 5 \times 10^{-3}$, setting the dust scale height at $H_d = \sqrt{D/\zeta} \approx 0.07$. This diffusion is applied only in the z direction. This anisotropic diffusion is chosen to provide support against gravity in the vertical direction, while not quenching the radial instability. It is also physically motivated. Because the processes that generate and/or shape turbulence are in general anisotropic (stratification, rotation, magnetic fields), turbulent diffusion is in general anisotropic as well[42,43]. In practice, the continuity equation has a diffusion term in the right hand side, $\boldsymbol{\nabla}\cdot\boldsymbol{J}$, where we substitute $\boldsymbol{J} = D\boldsymbol{\nabla}\rho$ (that yields the usual isotropic diffusion) by $\boldsymbol{J} = (\boldsymbol{D}\cdot\boldsymbol{\nabla})\rho_g$, with $\boldsymbol{D} = (0, 0, D)$.

To assess the evolution of the non-axisymmetric modes, we measured the power spectrum through the 3D simulation, which we show in Suppl. Fig. 5. Power in x, y, and z are shown in the upper, middle, and lower panel, respectively. Snapshots are shown at 5 (blue), 50 (red), and 100 orbits (black). The power in x shows the development of the instability, at $k_x \approx 60$, in agreement with the spacing between the stripes seen in Fig. 2 of the main article. The

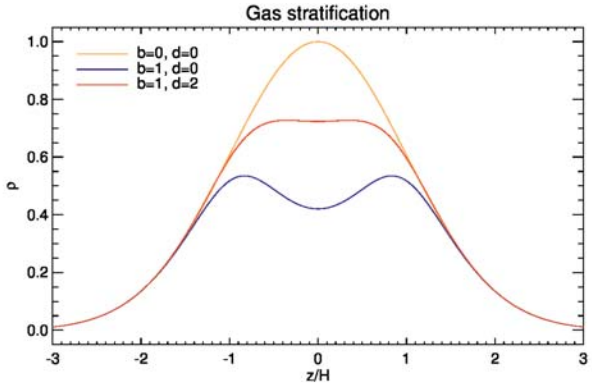

Supplementary Figure 4: Vertical stratification of gas, in the presence of different processes, for a column of dust of scale height H_d=0.5 (in the same units) maintained by diffusion. The parameters b and d represent the magnitudes of photoelectric heating and drag force backreaction, respectively. The dark yellow line is the usual isothermal Gaussian stratification. When photoelectric heating from the dust column is included, the center heats up and expands, leading to the double-peaked profiled shown as the blue line. With the extra heating, less mass is needed to balance the stellar gravity. The red line shows the equilibrium profile when drag backreaction is included. The dip in the center is filled because the backreaction causes gas to be dragged along with the settling dust, effectively behaving as extra gravity.

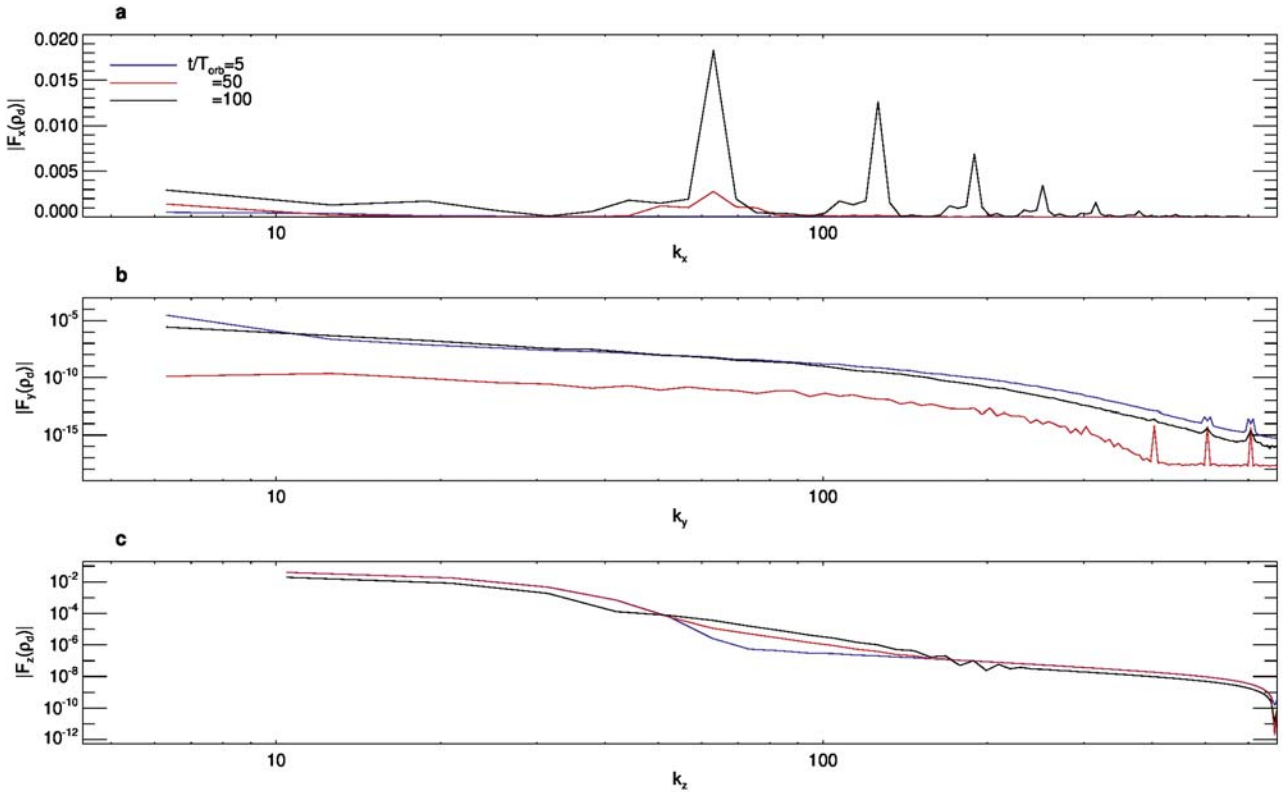

Supplementary Figure 5: Spectral power measured in the simulation shown in Fig. 2 of the main article. The power is shown in three snapshots, at 5, 50, and 100 orbits. **a**, The instability in x appears as the conspicuous spike at $k_x \approx 60$. Resonant instabilities at doubled wavenumbers are also apparent. **b**, The power in y behaves non-monotonically in time. It first drops from 5 to 50, then rises again from 50 to 100 back to levels close to the initial one. There is no evidence for nonaxisymmetric instability, as power remains concentrated in low k_y throughout the simulation. **c**, The power in z remains statistically constant in shape and magnitude, which reflects the stability of the stratification.

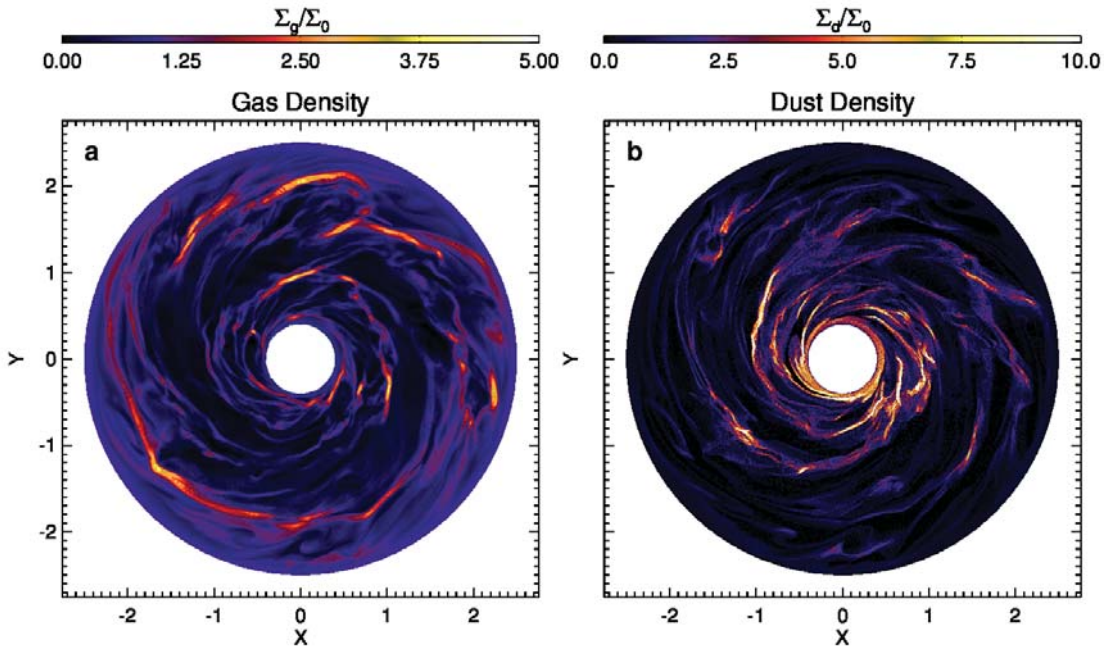

Supplementary Figure 6: Fifteen orbits into a version of the fiducial model shown in Fig. 3 of the main paper, but *without* the backreaction of the dragforce. Whereas the fiducial model develops into rings, this model breaks into several clumps. The backreaction is necessary to maintain the axisymmetry of the system, by resisting the tendency of the gas to counter-rotate in and around the regions of high pressure created by the dust.

difference in power at this wavenumber between 50 and 100 orbits is also in agreement with the time development of the instability as seen in Fig. 2c-d of the main article.

The power in z has remained roughly constant through the simulation. The power in y (middle panel), on the other hand, shows a decline from the initial noise, easily seen as the power drops five orders of magnitude from 5 to 50 orbits. After that, between 50 and 100 orbits, which coincides with the development of the instability (as seen in the x-power and Fig 2 of the main article), the azimuthal power is restored to the initial levels. We conclude that no short-wavelength non-axisymmetric instability is associated with photoelectric heating.

7 Excluding the drag force backreaction

We observe that the well-ordered scenario of the photoelectric instability gives way to turbulence when the drag force backreaction is excluded from the calculation. We show this case in Suppl. Fig. 6. This global simulation is similar to the fiducial case shown in the main paper in all aspects, except that the backreaction is switched off. As seen in the figure, axisymmetry is heavily broken, and the disk is teared apart into clumps. The drag force backreaction clearly has a pivotal role in maintaining axisymmetry. We encountered this before, when we noticed in Sect. 5.1.3 that the 1D particle streams were sharper and better confined when this term was included, though the effect is by far better appreciated in 2D.

This behavior stems from a disruption of geostrophy when the backreaction is introduced. When a dust overdensity generates a localized high pressure region, the motion initiated by the high pressure will be made to rotate by the influence of the Coriolis force. If backreaction is not present, the gas is free to execute this rotation, aware of the presence of dust only insofar as the latter influences the pressure. Nothing precludes the existence of several such clumps in the same orbit, and therefore azimuthal symmetry is not preferred.

When, however, the backreaction is included, the gas cannot revolve around freely anymore. If the gas crosses the dust overdensity from the inside outward, it is slowed down (if the dust concentration is low) or outright barred (if the dust density is high). Pressed from both sides, the dust will expand sideways, i.e., in azimuth. The overall tendency is therefore to smear the dust azimuthally (eventually towards a predominant $m = 0$ mode), and in the process keeping the gas and dust radially segregated.

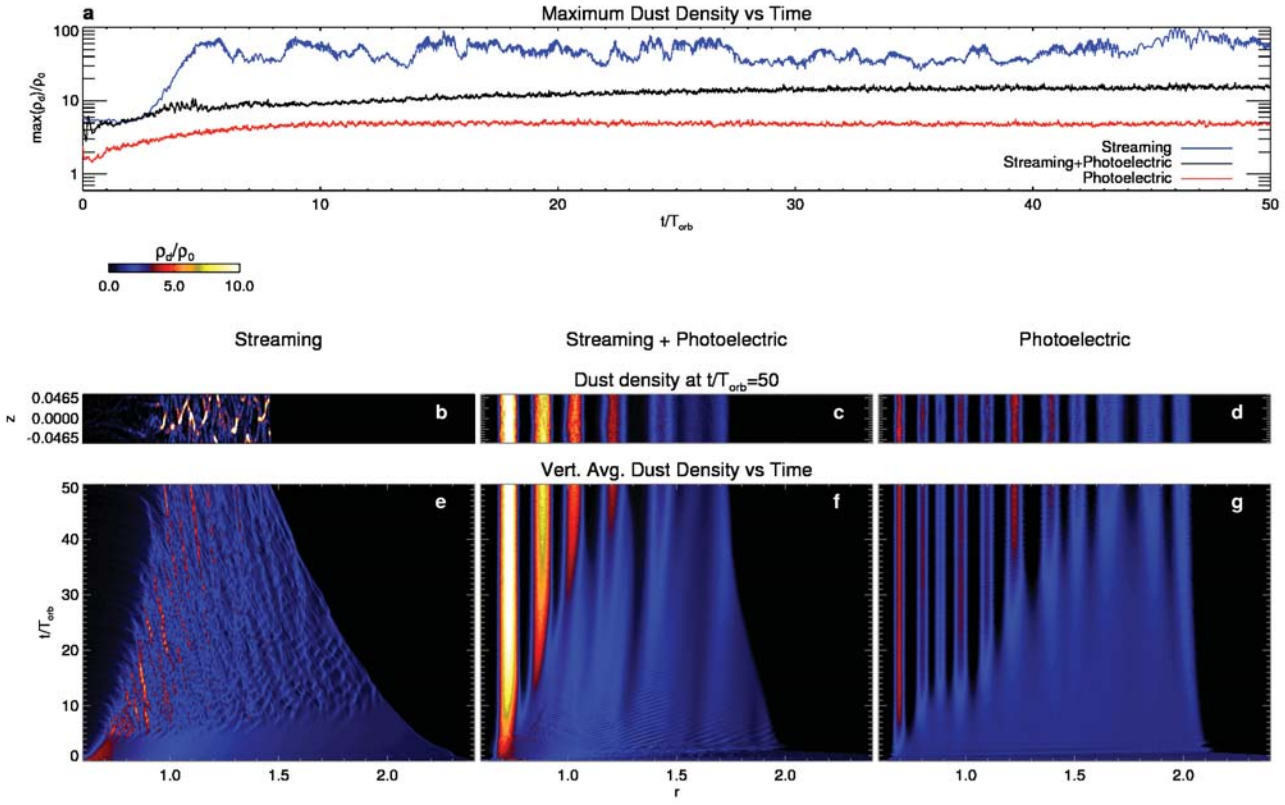

Supplementary Figure 7: Comparison between the streaming and photoelectric instabilities. **a**, The maximum dust density attained in the simulations. **b-d**, Snapshots of dust density in *r*-*z* of the models by the the end of the simulations at 50 orbits. **e-g**, The time-evolution of the 1D vertically averaged dust density. We reproduce both the streaming and photoelectric instabilities in isolation. When both are modeled together, the photoelectric instability dominates the dynamics.

8 Comparison with streaming instability

We have so far considered only disks for which the initial condition consist of gas in constant pressure. This choice was made in order to isolate the effect of photoelectric heating by shutting down the streaming instability[24,44–46], a traffic-jam clumping instability that is triggered when particles migrate (or "stream") through pressure-supported sub-Keplerian gas. The possibility exists then, that the proposed instability is overwhelmed by the streaming instability when realistic density and temperature gradients are used. We now examine this case, and show that in actuality the opposite is true.

We simulate the flow in the presence of a radial pressure gradient, that will trigger the streaming instability. The wavelength of interest is $\lambda_\eta = \eta r$, where η parametrizes the strength of the pressure gradient, according to[24]

$$\eta \equiv -\frac{1}{2\rho_g \Omega^2 r}\frac{\partial p}{\partial r} = -\frac{c_s^2}{2v_K^2}\frac{\partial \ln p}{\partial \ln r} \approx \left(\frac{c_s}{v_k}\right)^2. \tag{66}$$

Given the definition of the aspect ratio and scale height, this can be written $\eta r \approx h^2 r = hH$. We set a global disk in r and z, with radii ranging from 0.4 to 2.5. Gas and dust surface densities are initialized as power laws of index -1.5, which provides the streaming. The initial dust-to-gas ratio is $\varepsilon = 1$. We choose $h^2 = 0.1$ and use 768 points in r. The characteristic wavelength is therefore excellently resolved with 32 points. We use 32 points in z, with the same resolution as in radius to allow for growth of the streaming instability. Viscosity is added as $\alpha = 10^{-3}$. Four simulations are performed, switching on and off the pressure gradient and photoelectric heating. The result is shown in Suppl. Fig. 7.

The upper panel shows the time-series of the maximum dust density achieved in the simulation. The middle panels show the state of the $r-z$ flow at 50 orbits. The lower panels show the evolution of the vertically averaged dust density as a function of radius and time. The control model without pressure gradient or photoelectric heating is essentially constant in time and not shown.

In the simulation without heating but with the pressure gradient (lower left panels and blue line in upper panel), we recover the streaming instability, with clumps forming all over the grid and achieving high densities as they trap particles in their streaming course. When photoelectric heating is considered but not the pressure gradient (lower right panels and black line in upper panel), we recover the photoelectric instability, forming structures of longer wavelength in radius (about $\lambda = H/2$ in size), and symmetric in z. When both the pressure gradient and photoelectric heating are included, (lower middle panels and black line in upper panel), the maximum dust density achieved is bigger ($\approx \times 2$) than in the purely photoelectric case, but yet three to four times lower than in simulation with the streaming instability alone. The structures formed (middle lower panels) are of similar size as those generated in the case without the pressure gradient (right lower panels), and also symmetric in z. Overall, the result is intuitive. When the photoelectric effect is at play, gas is forced to rarefy in regions of high dust concentration, disrupting the pressure gradient responsible for the streaming. We conclude that it is the photoelectric mechanism, not the streaming instability, that dominates the dynamics.

9 Free oscillations

9.1 Long wavelength limit

We find in the simulations that the rings execute oscillations. The modes in question are the free, non-damped, oscillations that occur through most of the parameter space of Fig. 1a-c of the main article. We can find these modes analytically by taking the long wavelength limit ($n \to 0$). Ignoring the n terms, the system becomes a quartic equation,

$$A = 1; \quad B = 2\varepsilon + 2; \quad C = \varepsilon^2 + 2\varepsilon + 3;$$
$$D = 2\varepsilon + 2; \quad E = \varepsilon^2 + 2\varepsilon + 2; \quad F = 0;$$

which can be solved exactly. The roots are

$$\lim_{n\to 0} \sigma = \pm i; \quad \lim_{n\to 0} \sigma = -(\varepsilon + 1) \pm i \tag{67}$$

i.e., two solutions are free oscillations at wave frequency Ω, thus constituting epicyclic oscillations. The other two solutions are damped oscillations at the same frequency Ω, and damping time $(\varepsilon+1)^{-1}\Omega^{-1}$. The eigenvector corresponding to the $\sigma = \pm i$ solution represent the particular mode for which $\hat{v}_x = \hat{u}_x$ and $\hat{v}_y = \hat{u}_y$, therefore canceling the drag force. This epicyclic mode is low-k and non-damped, and should show up in the simulations as free oscillations.

We model a 1D system in the instantaneous thermal coupling approximation, as used in the linear analysis, where the equation of state is given by Eq. (11). The time evolution of the dust and gas densities is shown in Suppl. Fig. 8.

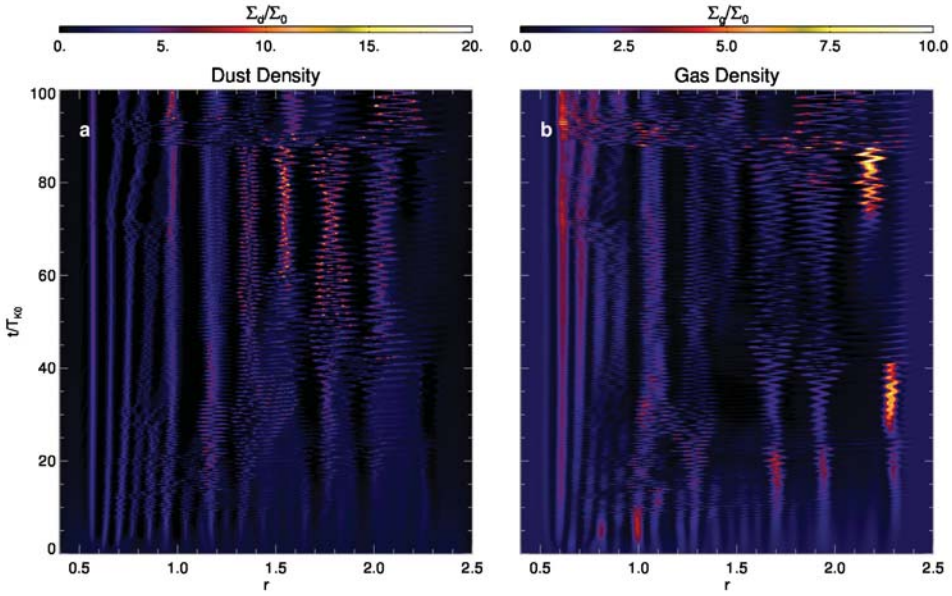

Supplementary Figure 8: Model with instantaneous thermal coupling between gas and dust. The gas (**a**) attains much denser concentrations, and the dust (**b**) executes high frequency oscillations. At later times the dust streams in the outer disk break into a roughly uniform sheet of dust extending from r=1.4 to r=2.0

The evolution looks a hybrid between the models considered in Sect. 5. On the one hand the dust streams are very thin, because of the shepherding provided by the drag force backreaction. On the other hand, the infinitesimally small thermal time leads to rapid wave excitation, seen in the high frequency oscillation of the dust.

We take a close look at this behavior, zooming into the dynamics of the stream. We show in Suppl. Fig. 9 the initial development of the instability (≈ 8 orbits) in a local box ranging $x = [-2.5, 2.5]H$ with 256 grid points, using both the Eulerian fluid and Lagrangian particle approaches. Viscosity is applied to the fluid and gas at $\alpha = 10^{-2}$. Fluid and particle approaches therefore sample different Reynolds numbers (Lagrangian particles are inviscid). The upper panels show the linear case, that the fluid approach (upper left) can capture. The particle simulation (upper right) will trigger the nonlinear regime, which is seen by the high amplitude in that case. Yet a similar wavelength was excited, which suggests linearity. The lower panels show the marginally nonlinear regime, at $\varepsilon = 1$. The fluid simulation (lower left) was quiescent in this case for linear noise, and had to be started at a noise level of 10% of the sound speed. The linear mode is also present, as seen in the underdense region developing in the middle of the figure, corresponding to the same density dip in the upper panel. This is because the dust was depleted in that region, falling below $\varepsilon = 1$. The particle simulation at the nonlinear regime (lower right) has the same overall wavelength as the fluid one, which is seen as the streams develop in the same location. However, the Reynolds number is different (essentially inviscid), which as a result leads to clearer oscillatory dynamics in the particle case. These are present in the fluid case as well, albeit less prominently. These oscillations are responsible for the non-zero eccentricity seen in two-dimensional models.

These modes are $\boldsymbol{u} = \boldsymbol{v}$ modes, that naturally occur at high dust-to-gas ratio, as dust drags the gas along. The question is therefore how to excite these modes. Excitation of the high-epsilon epicyclic mode is possible in the following way. If the orbits of the dust in the ring should happen to become slightly eccentric, ordinarily, gas drag would damp the eccentricity, by slowing the grains near pericenter and pushing the grains near apocenter forward. However, when gas is heated by the dust, the side of an eccentric ring that is closer to the star heats the gas more, increasing the gas pressure on that side. The resulting gradient in the gas pressure slows the gas orbital motion on one side of the ring, causing the gas streamlines to become eccentric as well, and therefore canceling the drag force, sustaining the mode. The azimuthal pressure gradient in turn attracts more dust, creating a tendency for apsidal alignment. Notice that this mechanism works best when $\tau_T \ll \tau_f$, i.e., when the thermal time is short in comparison to the friction time. This way, the gas in eccentricity excursion has time to heat up at the periapse and establish the pressure gradient. Otherwise, the gas drag has enough time to damp the dust attempt at eccentricity excursion back to the circular ring. This is precisely what we see in Suppl. Fig. 1 and Suppl. Fig. 8, as the oscillations only appear for short thermal time.

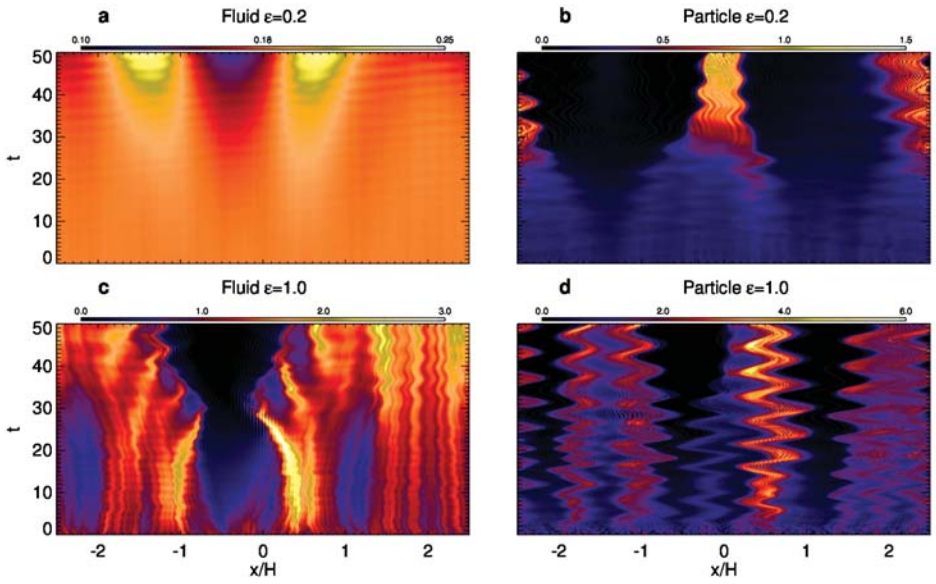

Supplementary Figure 9: Time series of the 1D dust density, showing the linear and marginally nonlinear development of the photoelectric instability in the initial $t = 50$ (≈ 8 orbits) of the simulations. **a-b**, In the $\varepsilon = 0.2$ case there is linear instability, which is retrieved in both cases. **c-d**, In the $\varepsilon = 1$ case there is only nonlinear instability. The fluid simulation shown in the lower left panel had to be started with noise at $u_{\rm rms} = 0.1\,c_s$, since for linear noise it is quiescent. The particle simulation at $\varepsilon = 1$ develops epicylic oscillations (period $= 1/\Omega = 2\pi$), also visible in the fluid approach but less clear due to the higher Reynolds number.

References

[31] Zagorovsky, K., Brandeker, A., & Wu, Y. Gas Emission from Debris Disks Around A and F Stars. *Astrophys. J.*, **720**, 923-939, (2010).

[32] Thi, W.F., Blake, G.A., van Dishoek, E.F. et al. Substantial reservoirs of molecular hydrogen in the debris disks around young stars. *Nature*, **409**, 60-63, (2001).

[33] Hughes, A. M., Wilner, D. J., Kamp, I., & Hogerheijde, M. R. A Resolved Molecular Gas Disk around the Nearby A Star 49 Ceti. *Astrophys. J.*, **681**, 626-635, (2008).

[34] Nilsson, R., Brandeker, A., Olofsson, G., Fathi, K., Thébault, Ph., Liseau, R. VLT imaging of the β Pictoris gas disk. *Astron. Astrophys.*, **544**, 134-145, (2012).

[35] Freudling, W., Lagrange, A.-M., Vidal-Madjar, A., Ferlet, R., Forveille, T. Gas around β Pictoris: an upper limit on the HI content. *Astron. Astrophys.*, **301**, 231-235, (1995).

[36] Fitzgerald, M. P., Kalas, P. G., & Graham, J. R. A Ring of Warm Dust in the HD 32297 Debris Disk. *Astrophys. J.*, **670**, 557-564, (2007).

[37] McNally, C. P., Lyra, W., & Passy, J.-C. A Well-posed Kelvin-Helmholtz Instability Test and Comparison. *Astrophys. J. Suppl.*, **201**, 18-34, (2012).

[38] Hawley, J. F., Gammie, C. F., & Balbus, S. A. Local Three-dimensional Magnetohydrodynamic Simulations of Accretion Disks *Astrophys. J.*, **440**, 742-763, (1995).

[39] Brandenburg, A., Nordlund, Å., Stein, R. F., & Torkelsson, U. Dynamo-generated Turbulence and Large-Scale Magnetic Fields in a Keplerian Shear Flow. *Astrophys. J.*, **446**, 741-754, (1995).

[40] Dubrulle, B., Morfill, G., & Sterzik, M. The dust subdisk in the protoplanetary nebula. *Icarus*, **114**, 237-246, (1995).

[41] Johansen, A. & Klahr H. Dust Diffusion in Protoplanetary Disks by Magnetorotational Turbulence. *Astrophys. J.*, **634**, 1535-1371, (2005).

[42] Johansen, A., Klahr, H., & Mee, A. J. Turbulent diffusion in protoplanetary discs: the effect of an imposed magnetic field. *mnras*, **370**, L71-L75, (2006).

[43] Brandenburg, A., Svedin, A., & Vasil, G. M. Turbulent diffusion with rotation or magnetic fields. *Mon. Not. R. Astron. Soc.*, **395**, 1599-1606, (2009).

[44] Youdin, A. N. & Goodman, J. Streaming Instabilities in Protoplanetary Disks. *Astrophys. J.*, **620**, 459-469, (2005).

[45] Johansen, A. & Youdin, A. Protoplanetary Disk Turbulence Driven by the Streaming Instability: Nonlinear Saturation and Particle Concentration. *Astrophys. J.*, **662**, 627-641, (2007).

[46] Jacquet, E., Balbus, S. & Latter, H. On linear dust-gas streaming instabilities in protoplanetary discs. *Mon. Not. R. Astron. Soc.*, **415**, 3591-3598, (2011).